9-9-2015

Self-Accleration and Instability of Gravity Wave Packets: 1. Effects of Temporal Localization

David C. Fritts
GATS Inc. Boulder Division, Boulder, Colorado

Brian Laughman
GATS Inc. Boulder Division, Boulder, Colorado

Thomas S. Lund
Colorado Research Associates Division, NorthWest Research Associates, Boulder, Colorado

Jonathan B. Snively
Embry-Riddle Aeronautical University, snivelyj@erau.edu

Scholarly Commons Citation

Fritts, D. C., B. Laughman, T. S. Lund, and J. B. Snively (2015), Self-acceleration and instability of gravity wave packets: 1. Effects of temporal localization, J. Geophys. Res. Atmos., 120, 8783–8803, doi:10.1002/2015JD023363.

AGU PUBLICATIONS

JGR

Journal of Geophysical Research: Atmospheres

RESEARCH ARTICLE

10.1002/2015JD023363

Key Points:

- Gravity wave self-acceleration dynamics are common in the atmosphere
- Self-acceleration disrupts gravity wave vertical propagation
- Self-acceleration leads to instabilities and local momentum deposition

Correspondence to:
D. C. Fritts,
dave@gats-inc.com

Citation:
Fritts, D. C., B. Laughman, T. S. Lund, and J. B. Snively (2015), Self-acceleration and instability of gravity wave packets: 1. Effects of temporal localization, *J. Geophys. Res. Atmos.*, *120*, 8783–8803, doi:10.1002/2015JD023363.

Received 11 MAR 2015
Accepted 22 JUL 2015
Accepted article online 25 JUL 2015
Published online 9 SEP 2015

Self-acceleration and instability of gravity wave packets: 1. Effects of temporal localization

David C. Fritts[1], Brian Laughman[1], Thomas S. Lund[2], and Jonathan B. Snively[3]

[1]GATS Inc. Boulder Division, Boulder, Colorado, USA, [2]Colorado Research Associates Division, NorthWest Research Associates, Boulder, Colorado, USA, [3]Department of Physical Sciences, Embry-Riddle Aeronautical University, Daytona Beach, Florida, USA

Abstract An anelastic numerical model is used to explore the dynamics accompanying the attainment of large amplitudes by gravity waves (GWs) that are localized in altitude and time. GW momentum transport induces mean flow variations accompanying a GW packet that grows exponentially with altitude, is localized in altitude, and induces significant GW phase speed, and phase, variations across the GW packet. These variations arise because the GW occupies the region undergoing accelerations, with the induced phase speed variations referred to as "self-acceleration." Results presented here reveal that self-acceleration of a GW packet localized in time and altitude ultimately leads to stalling of the vertical propagation of the GW packet and accompanying two- and three-dimensional (2-D and 3-D) instabilities of the superposed GW and mean motion field. The altitudes at which these effects occur depend on the initial GW amplitude, intrinsic frequency, and degree of localization in time and altitude. Larger amplitudes and higher intrinsic frequencies yield strong self-acceleration effects at lower altitudes, while smaller amplitudes yield similar effects at higher altitudes, provided the Reynolds number, *Re*, is sufficiently large. Three-dimensional instabilities follow 2-D "self-acceleration instability" for sufficiently high *Re*. GW packets can also exhibit self-acceleration dynamics at more than one altitude because of continued growth of the GW packet leading edge above the previous self-acceleration event.

1. Introduction

Gravity waves (GWs) arise from various sources in the lower atmosphere, the most significant of these being convection, airflow over orography, frontal systems, and jet streams [e.g., *Fritts and Nastrom*, 1992; *Fritts and Alexander*, 2003; *Kim et al.*, 2003, and references therein]. Additional sources at higher altitudes include auroral heating, nonlinear interactions, instability dynamics, and body forces due to local GW momentum transport and dissipation [e.g., *Mayr et al.*, 1990; *Luo and Fritts*, 1993; *Hocke and Schlegel*, 1996; *Vadas and Fritts*, 2002, 2004; *Fritts et al.*, 2002, 2009a, 2013]. Each source yields a spectrum of GW spatial scales and intrinsic frequencies that depend on the source characteristics and the environment in which it occurs. GWs arising from these various sources and maintaining sufficiently high intrinsic phase speeds and vertical group velocities thereafter may propagate into the mesosphere and lower thermosphere (MLT) or higher [*Hocke and Schlegel*, 1996; *Mendillo et al.*, 1997; *Oliver et al.*, 1997; *Djuth et al.*, 1997, 2004; *Innis et al.*, 2001; *Innis and Conde*, 2002; *Abdu et al.*, 2009; *Vadas and Nicolls*, 2009]. In such cases, GW amplitude growth with increasing altitude can be dramatic, yielding amplitudes and momentum fluxes (per unit density) that can be several or many decades larger than near the GW source [e.g., *Vadas*, 2007; *Fritts and Vadas*, 2008; *Fritts and Lund*, 2011, hereafter FL11]. These various dynamics have global implications extending into the thermosphere [e.g., *Oberheide et al.*, 2015; *Yiğit and Medvedev*, 2015], but their parameterizations in global models remain simplistic at present [*Kim et al.*, 2003].

The importance and roles of GWs in the MLT and higher in the thermosphere and ionosphere (TI) have become increasingly recognized and quantified over the half century since the identification of their signatures in ionospheric irregularities by *Hines* [1960]. Indeed, we now understand many of their more significant effects in the MLT. However, our understanding of their TI effects is much more limited at present. Dynamical effects in the MLT include the following: (1) GW breaking, interactions, instability, and turbulence leading to GW dissipation and momentum flux divergence [e.g., *Lindzen*, 1981; *Fritts et al.*, 1988, 1993, 2002, 2009a, 2009b, 2013; *Andreassen et al.*, 1998; *Achatz*, 2005, 2007; *Horinouchi et al.*, 2002; *Snively and Pasco*, 2003; *Fruman et al.*, 2014]; (2) closure of the mesospheric jets at middle and high latitudes accompanying momentum deposition and body forcing that oppose the zonal mean winds [e.g., *Lindzen*, 1981; *Holton*, 1982, 1983;

Vincent and Reid, 1983; *Garcia and Solomon*, 1985; *Tsuda et al.*, 1990; *Gavrilov et al.*, 2000]; (3) an induced residual circulation near the mesopause, with mean meridional motions from the summer to the winter hemisphere and downward (upward) motions and warming (cooling) at high latitudes in winter (summer) [e.g., *Haynes et al.*, 1991; *Nastrom et al.*, 1982; *Garcia and Boville*, 1994; *Fritts and Alexander*, 2003]; and (4) interactions with tides and planetary waves having feedbacks on these motions and potentially mapping these structures to higher altitudes [e.g., *Walterscheid*, 1981; *Holton*, 1984; *Fritts and Vincent*, 1987; *Miyahara and Forbes*, 1991; *Wang and Fritts*, 1991; *Lu and Fritts*, 1993; *McLandress and Ward*, 1994; *Smith*, 1996; *Meyer*, 1999a, 1999b; *Preusse et al.*, 2001; *Ortland and Alexander*, 2006; *Liu et al.*, 2008].

Based on the limited observational, theoretical, and modeling studies performed to date, GW responses and dynamical effects in the TI are believed to include the following: (1) strong viscous damping of GWs in the thermosphere, causing increases in characteristic scales with increasing altitude [e.g., *Pitteway and Hines*, 1963; *Oliver et al.*, 1997; *Vadas and Fritts*, 2005; *Fritts and Vadas*, 2008; *Yiğit and Medvedev*, 2010; *Heale et al.*, 2014; *Gavrilov and Kshevetskii*, 2015]; (2) attainment of amplitudes that may become large and have implications for neutral and plasma dynamics at high altitudes [e.g., *Hocke and Schlegel*, 1996; *Abdu et al.*, 2009; *Vadas and Liu*, 2009]; (3) significant momentum transport and deposition by primary GWs arising in the lower atmosphere and secondary GWs generated at higher altitudes [e.g., *Vadas and Fritts*, 2002; *Vadas*, 2007; *Yiğit et al.*, 2008, 2009, 2014; *Vadas and Liu*, 2011, 2013]; and (4) generation of instabilities and turbulence extending well into the thermosphere accompanying large GW amplitudes and momentum deposition [e.g., *Lund and Fritts*, 2012, hereafter LF12].

Given the evidence for large amplitudes and momentum fluxes, and transience of large-scale GWs in the MLT and TI, we expect that nonlinear effects, including transient responses and instabilities, must play significant, but largely unknown, roles in GW dynamics at these altitudes. Indeed, GWs exhibit interactions and instabilities at small and large amplitudes that can cause large departures from linear behavior and influence the evolution of the GW spectrum in altitude [e.g., *Whitham*, 1965, 1974; *Hasselmann*, 1967; *Grimshaw*, 1975, 1977; *Mied*, 1976; *McComas and Bretherton*, 1977; *Lighthill*, 1978; *Yeh and Liu*, 1981; *Müller et al.*, 1986; *Klostermeyer*, 1991; *Vanneste*, 1995; *Lombard and Riley*, 1996; *Sonmor and Klaassen*, 1997; *Sutherland*, 1999, 2001, 2006a, 2006b; *Dosser and Sutherland*, 2011].

Early studies of GWs that are localized in the vertical revealed various responses to transient GW momentum transport. *Dunkerton* [1981] and *Fritts and Dukerton* [1984] showed that "self-acceleration" (hereafter SA, e.g., acceleration of the GW horizontal phase speed due to its residence in the region undergoing mean flow acceleration in the direction of GW propagation caused by transient momentum flux divergence) can increase the GW phase speed in the direction of GW propagation at the leading edge of a wave packet (e.g., where the GW amplitude and momentum flux (per unit density) increase rapidly at a given altitude), enabling higher GW packet propagation in shear and penetration above an initial critical level. More recent studies [e.g., *Fritts et al.*, 1996] showed transient induced flows in a mean shear to become permanent due to dissipation and to enhance mean shears at the trailing edge of the wave packet. *Sutherland* [2001] employed the Boussinesq fluid equations to infer that a GW packet localized in the vertical will be unstable to overturning if the induced mean flow exceeds the GW horizontal group velocity (e.g., "SA instability") and that SA effects can occur at small GW amplitudes if the intrinsic frequency is close to the buoyancy frequency, e.g., $\omega_i > 0.82N$. *Sutherland* [2006a] employed Boussinesq theory and modeling to show both (1) that GW packets that are suitably localized vertically and have sufficiently high ω_i become unstable to SA effects rather than parametric instabilities and (2) that GW packets having $\lambda_{z0} > 2^{1/2}\lambda_x$ (e.g., the GW with the largest vertical group velocity for given horizontal wave number), where λ_{z0} and λ_x are the initial vertical wavelength and horizontal wavelength, will also exhibit modulational instabilities.

We expect SA dynamics to have important influences in the atmosphere and that density decreases with altitude will accelerate leading edge effects for deep packets (e.g., packet widths greater than a scale height) relative to a Boussinesq fluid. Specifically, SA dynamics will depend on GW amplitude variations due to the packet profile and GW amplitude growth with altitude accompanying decreasing density. More generally, GW packets that are localized in two or three dimensions must also exhibit SA dynamics, but their effects will depend on the GW parameters and the degree and character of spatial localization of the GW packet.

Initial studies of these mean flow interaction and instability dynamics for transient GWs in an idealized atmosphere with density scale height H were performed by *Dosser and Sutherland* [2011], FL11, and LF12.

These studies revealed that both localized GW packets and GWs approaching a constant amplitude at the forcing level exhibit large mean flow accelerations at higher altitudes that impact the GW structure and dynamics thereafter. *Dosser and Sutherland* [2011] showed that anelastic GW packets are modulationally unstable for $\lambda_{z0}/\lambda_x > 2^{1/2}[1+\lambda_x{}^2/(4\pi H)^2]^{-1/2}$ and examined the nonlinear evolutions of Gaussian GW packets that were modulationally stable and unstable. The results showed that modulational instability causes overturning below the altitude of overturning predicted by linear theory (i.e., z_{break}), whereas modulational stability causes GWs to penetrate to altitudes above z_{break} prior to overturning. A Gaussian GW packet having larger λ_x and λ_{z0}, but smaller packet width than assumed by *Dosser and Sutherland* [2011], was found by FL11 to exhibit (1) amplitude growth by ~2000 times from 0 to ~130 km, (2) strong SA leading to large GW phase distortions, (3) stalling of the vertical propagation of the GW, and (4) evidence of SA instability accompanying large mean flow accelerations. Applications of these dynamics to the parameterization of mountain wave momentum deposition were examined.

Simulations of a GW approach to steady forcing by LF12 revealed very different GW and instability evolutions for cases including induced mean flows and with induced mean flows suppressed. The former is a reasonable approximation for a GW that is highly extended horizontally; the latter is likely more representative of observations of GWs already altered by the induced mean motions or for highly localized forcing. A simulation in which induced mean flows were suppressed exhibited GW breaking and 3-D instabilities extending to high altitudes at large vertical GW scales. These dynamics resulted in significant GW amplitude reductions, with instabilities occurring at lower altitudes and smaller spatial scales with time, but allowed the remaining GW to continue to propagate to higher altitudes. A second simulation allowing induced mean flows enabled strong mean flow accelerations at higher altitudes during GW amplitude growth that constrained GW breaking and instability to much lower altitudes and smaller vertical scales initially and increasingly with time.

This study builds on the initial 2-D simulation of propagation and SA of a localized GW packet in a deep atmosphere described by FL11. The anelastic equations and finite-volume (FV) model setup for the various simulations performed are described in section 2. Effects of transient mean flow accelerations and varying GW amplitudes, wavelengths, packet depths, initial intrinsic frequencies, and Reynolds numbers on GW SA dynamics are described in section 3. Section 4 provides a summary and discussion of these results and our conclusions.

2. FV Model and Simulations

2.1. Anelastic Equations

As in LF12, we solve the anelastic equations originally suggested by *Lipps and Hemler* [1982] and clarified by *Lipps* [1990] and *Bannon* [1996]. This formulation involves retaining density fluctuations only in the buoyancy term (e.g., the Boussinesq approximation). The thermodynamic definition of the potential temperature fluctuation is also modified to achieve an equation set that conserves mass, momentum, total energy, and potential vorticity, apart from dissipative effects. This system also yields a GW dispersion relation in a nonrotating, isothermal atmosphere that agrees with the low-frequency branch of the compressible acoustic GW dispersion relation [*Bannon*, 1996]. These equations can be written as [LF12]

$$\frac{\partial \bar{\rho} u_j}{\partial x_j} = 0 \tag{1}$$

$$\frac{\partial \bar{\rho} u_i}{\partial t} + \frac{\partial \bar{\rho} u_i u_j}{\partial x_j} = -\frac{\partial p'}{\partial x_i} + \left(\frac{\bar{\rho}\theta' g}{\theta} - \frac{p'}{H}\right)\delta_{i3} + \frac{\partial}{\partial x_j}\left[\mu\left(\frac{\partial u_i}{\partial x_j} + \frac{\partial u_j}{\partial x_i}\right)\right] \tag{2}$$

$$\frac{\partial \bar{\rho}\theta}{\partial t} + \frac{\partial \bar{\rho}\theta u_j}{\partial x_j} = \frac{\overline{\theta}}{c_p \overline{T}}\left[\mu\left(\frac{\partial u_i}{\partial x_j} + \frac{\partial u_j}{\partial x_i}\right)\frac{\partial u_i}{\partial x_j} - \frac{\partial}{\partial x_j}\left(\kappa \frac{\partial T}{\partial x_j}\right)\right] \tag{3}$$

Here overbars denote mean fields, primes denote deviations from these fields (e.g., $p' = p - \bar{p}$), and the solution variables are the velocity, u_i or (u, v, w), the pressure fluctuation, p', and the potential temperature fluctuation, θ'. The three coordinate directions are $i = 1, 2, 3$ or (x, y, z), and gravity, g, is aligned in the z direction. Molecular viscosity and thermal diffusivity are denoted by μ and κ, respectively, and these depend on the temperature through Sutherland's law [*White*, 1974]. The specific heat at constant pressure and the

Kroneker delta are denoted c_p and δ_{ij}. Note that hydrostatic balance has been removed from the momentum equation and that the anelastic definition of the θ' fluctuation

$$\frac{\theta'}{\overline{\theta}} = -\frac{\rho'}{\overline{\rho}} + \frac{p'}{\overline{\rho} gH} \tag{4}$$

has been used to replace ρ' with θ' and p', and the density scale height is defined as

$$H = -\left(\frac{1}{\overline{\rho}}\frac{d\overline{\rho}}{\mathrm{d}z}\right)^{-1} \tag{5}$$

Finally, the temperature is determined through a linearized form of the ideal gas law,

$$\frac{T'}{\overline{T}} = \frac{p'}{\overline{p}} - \frac{\rho'}{\overline{\rho}} = \frac{\theta'}{\overline{\theta}} + \frac{p'}{\overline{p}}\left(1 - \frac{\overline{p}}{\overline{\rho} gH}\right) \tag{6}$$

Initial GW perturbations are assumed to have the form $\phi' = \phi_0' \exp[i(kx + m_0 z - \omega_0 t)]$, where $k = 2\pi/\lambda_x$ and $m_0 = 2\pi/\lambda_{z0}$ are the horizontal and initial vertical wave numbers, λ_x and λ_{z0} are the horizontal and initial vertical wavelengths, and $\omega_0 = kc_0$ and c_0 are the initial frequency and phase speed in the domain frame of reference. Assuming that GWs propagate in the (x,z) plane, the above equations yield a dispersion relation for evolving linear, inviscid GWs in a nonrotating, isothermal atmosphere that agrees with the GW branch of the compressible acoustic GW dispersion relation, expressing the intrinsic frequency, $\omega_i = k(c - U(z))$, as

$$\omega_i^2 = \frac{k^2 N^2}{k^2 + m^2 + 1/4H^2} \tag{7}$$

Nonzero kinematic viscosity and thermal diffusivity will alter the dispersion and polarization relations increasingly with altitude, but these have small influences for large GW scales and at lower altitudes. Large GW λ_z do influence the GW velocity field relative to motions for which $\lambda_z \ll 4\pi H$, however. These effects result in a velocity ratio given by

$$\frac{u'}{w'} = -\frac{m}{k}\left(1 + \varepsilon^2\right)^{1/2} \frac{\sin(\phi + \phi_1)}{\sin(\phi)} \tag{8}$$

where $\varepsilon = 1/2mH = \lambda_z/4\pi H$, $\phi = kx + m_0 z - \omega_0 t$, and $\phi_1 = \tan^{-1} \varepsilon$ (LF12). These relations imply both (1) shallower parcel orbits and a small phase difference between u' and w' that are responsible for the Stokes drift due to GWs in a compressible atmosphere and (2) the asymmetry in the spanwise vorticity magnitudes, $|\zeta_y|$, to be discussed below.

2.2. Anelastic FV Model

A second-order, finite-volume scheme identical to the method discussed by *Felten and Lund* [2006] is used to discretize the anelastic equations, yielding an anelastic FV model that results in exact numerical conservation of mass, momentum, and kinetic and thermal energy (apart from explicit dissipation) and thus faithfully represents the underlying conservation laws. A consequence of energy conservation is that the scheme has no numerical dissipation.

FV simulations discussed below are performed in a Cartesian computational domain that is periodic in the horizontal with initial 2-D GWs assumed to propagate in the streamwise-vertical (x,z) plane. The streamwise extent of the domain is taken to be two horizontal wavelengths of the primary GW. Three-dimensional simulations addressing instability dynamics accompanying 2-D GWs include a spanwise dimension (y) that is also assumed to be periodic. In these cases, the spanwise domain extent is taken to be sufficiently large (20 km in each case) to not constrain the instability scales that arise. As discussed more extensively by LF12, we note that the assumption of horizontal periodicity in the streamwise direction offers clear numerical advantages in terms of accuracy and computational efficiency. However, it also artificially constrains the spectrum of motions that can arise from nonlinear interactions and instability dynamics. Assuming, as we do here, that the initial GW has large horizontal extent, periodicity is not a strong constraint. But it does impose a discrete rather than a continuous spectrum of larger-scale motions that can result [see, e.g., *Franke and Robinson*, 1999; *Fritts et al.*, 2009a, 2013]. In particular, it prevents exploration of the horizontal contributions to the Eliassen-Palm fluxes and divergence that accompany a GW packet that is localized in 2-D or 3-D without a very large computational domain. These dynamics will be addressed in follow-on papers specifically addressing GW packets that are localized in 2-D and 3-D in large domains.

Table 1. GW Parameters for Each Case Discussed

Case	λ_x (km)	λ_{z0} (km)	T_{GW} (s)	ω_{i0} (*N*)	c_{i0} (m s^{-1})	u_0' (m/s)	z_0 (km)	z_{break} (km)	σ_0 (km)	2-D	3-D	d*U*/d*t* ≠ 0	*Z* (km)	Δ*x*, Δ*z* (m)
1	20	20	450	1/1.43	44.4	0.089	20	107	20		X	N	160	104,104
2	20	20	450	1/1.43	44.4	0.089	20	107	20		X	Y	160	104,104
3	20	20	450	1/1.43	44.4	2.66	60	99	20	X		Y	160	26,26
4	20	20	450	1/1.43	44.4	2.66	10	49	20	X		Y	160	26,26
5	10	10	446	1/1.42	22.4	0.25	20	83	20	X		Y	200	208,260
6	20	20	450	1/1.43	44.4	0.49	20	83	20	X		Y	200	208,260
7	40	40	468	1/1.49	85.7	0.94	20	83	20	X		Y	200	417,260
8	10	10	446	1/1.42	22.4	0.25	20	83	10	X		Y	200	208,260
9	20	20	450	1/1.43	44.4	16.7	50	64	10	X		Y	160	208,208
10	20	11.6	628	1/2	31.8	16.6	50	59	10	X		Y	160	208,208
11	20	7.1	942	1/3	21.2	16.5	50	53	10	X		Y	160	208,208
12	20	5.17	1256	1/4	15.9	16.4	50	50	10	X		Y	160	52,52
13	10	10	446	1/1.42	22.4	0.025	60	123	10		X	Y	220	52,69

The computational domains extend over 160, 200, or 220 km, depending on the altitudes of expected SA responses. Over these depths, the GW amplitudes and momentum fluxes (per unit density) increase by orders of magnitude, with the corresponding Reynolds number, $Re = c\lambda_z/\nu = \lambda_z^2/\nu T_b$ (where c, λ_z, $\nu = \mu/\rho$, and T_b are the GW phase speed, vertical wavelength, kinematic viscosity, and buoyancy period), decreasing exponentially with altitude. GW amplitudes, wavelengths, intrinsic frequencies, and initial altitudes are varied to explore the influences on SA dynamics. Specific GW and direct numerical simulation (DNS) parameters are provided in Table 1 for all DNS discussed below.

A radiation condition is imposed at the upper boundary that is an anelastic extension of the *Klemp and Durran* [1983] method, modified such that the required polarization relations are assessed from the computed solution near the upper boundary rather than being specified a priori. This modification allows the radiation condition to indirectly account for viscous and nonlinear effects near the upper boundary, which can lead to polarization relations that differ significantly from the predictions of linear inviscid theory.

GWs are introduced via harmonic perturbations in u', w', θ', ρ', and p' in a Gaussian density-weighted amplitude envelope specified using the GW polarization relations. The GW packet is defined by spatial variability of the imposed perturbation fields having the form

$$\bar{\rho}^{1/2}u'(z) = \exp\left[-\frac{(z-z_0)^2}{2\sigma_0^2}\right]\exp[\mathrm{i}(k_0x + m_0z - \omega_0t)] \tag{9}$$

such that the GW momentum flux is given by

$$\bar{\rho} < u'w' > = |\bar{\rho} < u'w' >|_{\max}\exp\left[-\frac{(z-z_0)^2}{\sigma_0^2}\right] \tag{10}$$

Here z_0 and σ_0 are the altitude of maximum initial momentum flux and the standard deviation of the GW amplitude distribution prior to refraction that determines the packet depth, angle brackets denote phase averaging over the GW, and the standard deviation of momentum flux is $\sigma_{MF} = \sigma_0/2^{1/2}$. The spatial localization in equation (9) yields a GW packet with multiple cycles for $\sigma_0 \sim \lambda_z$ or larger, implying a relatively narrow range of vertical wave numbers and relatively weak packet dispersion accompanying vertical propagation. Nevertheless, dispersion does play a role in the occurrence of instability, particularly for GW packets that evolve over large depths or have small relative widths.

For the ease of comparison of the different cases with key dynamics occurring at different altitudes, we choose a uniform temperature profile, $T(z) = 240$ K, and a uniform initial mean wind opposite to the GW propagation, $U(z) = -c_i$, allowing the GW phase to be nearly stationary ($c \sim 0$) in the absence of SA. For westward GW propagation, the mean wind is eastward initially but is either decelerated or accelerated accompanying GW momentum flux divergence due to transience, with these effects becoming permanent accompanying dissipation. The choice of $T(z)$ yields a scale height $H = 7$ km, a buoyancy frequency $N = 0.02$ s^{-1}, and $T_b = 2\pi/N = 314$ s. We also assume a true kinematic viscosity $\nu \sim 1.5 \times 10^{-5}$ m^2 s^{-1} at the Earth's surface, implying $\nu \sim 1.3$ and ~400 m^2 s^{-1} at altitudes of 80 and 120 km and *Re* decreasing by ~300 between these altitudes.

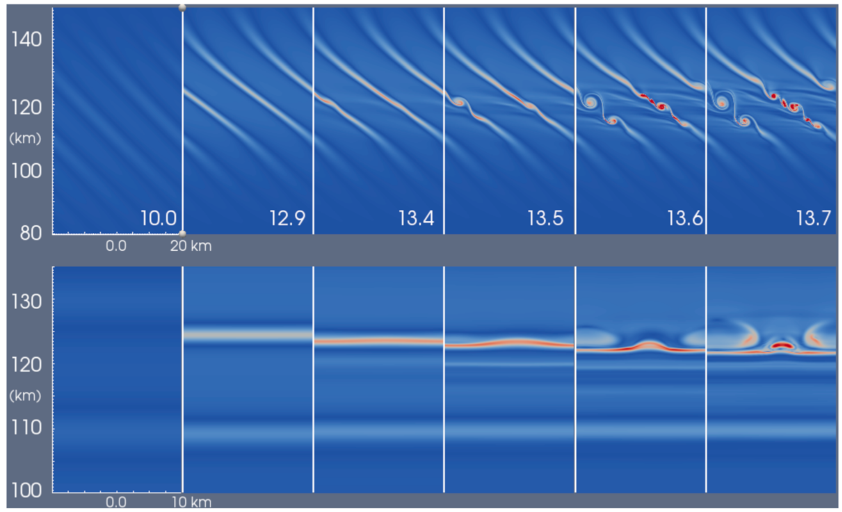

Figure 1. Time series of (top row) streamwise and (bottom row) spanwise cross sections of $|\zeta_y'|$ for Case 1. Times shown at the bottom right in Figure 1 (top row) are in T_b. Blue and red show minimum and maximum $|\zeta_y'|$, and the streamwise and spanwise domain extents are 40 and 20 km, respectively (see axis labels at the bottom of Figure 1, first column).

2.3. FV Model Simulations

GWs in most cases are assumed to have a horizontal wavelength of $\lambda_x = 20$ km, given our expectation that GWs with shorter horizontal wavelengths and higher phase speeds (and vertical wavelengths) are more likely to exhibit SA effects. The initial GW and packet parameters, domain depths and resolutions, whether the DNS is 2-D or 3-D (denoted by an "X"), whether the mean flow is allowed to evolve (dU/dt "Y" or "N"), and the grid resolutions, Δx and Δy, are listed for each case to be discussed in Table 1. In all cases, we display results for a doubly periodic domain having a streamwise dimension $X = 2\lambda_x$ so as to display the phase structures and their variations with altitude more clearly.

3. Simulation Results

Our primary purpose in this section is to examine the dependence of 2-D and 3-D GW self-acceleration (SA) dynamics on GW amplitude, intrinsic frequency, horizontal wavelength, *Re*, and packet depth for values of these quantities that we consider to be representative of high-frequency GWs in the MLT. In all cases, we assume initial GW propagation upward and to the west (with positive x to the west), such that $u'/w' > 0$ prior to phase distortions due to GW SA. We begin by illustrating the main differences in the dynamics between a GW that undergoes SA and one for which the mean flow is constrained to not change in space or time, as is assumed in linear theory and all GW parameterization schemes known to us except that recently proposed by *Scinocca and Sutherland* [2010]. GW parameters for the each of the DNS addressing these dynamics are listed for reference in Table 1.

3.1. GW and Mean Flow Evolutions, Instabilities, and Dissipation

Two DNS are performed to illustrate the differences between GW packet evolutions without and with SA influences on GW phase structure. GW parameters for these DNS are listed as Cases 1 and 2 in Table 1. These DNS are illustrated with streamwise-vertical and spanwise-vertical (hereafter streamwise and spanwise) cross sections of spanwise vorticity magnitude, $|\zeta_y'|$ (e.g., $\zeta_y' = \partial u'/\partial z - \partial w'/\partial x$), at 6 times spanning 3.7 and 5.2 T_b (~2.6 and 3.8 T_{GW}), respectively, in Figures 1 and 2. We use $|\zeta_y'|$ here because it provides a clearer distinction between these dynamics than the velocity or θ' fields. Figure 3 shows cross sections of u', w', $|\zeta_y'|$, and θ' (top to bottom) at 3 times (the final time) for the streamwise (spanwise, zoomed view) cross sections for Case 2 to illustrate the different SA signatures in these fields. Vertical profiles of the induced mean flow for Case 2 and momentum fluxes, $\rho_0 \langle u'w' \rangle$, for both cases spanning these times are shown in Figure 4. Examination of Figures 1–4 reveals strong differences between the two cases in (1) the primary GW phase structure and vertical propagation, (2) the occurrence and form of instabilities that arise, and (3) the rate of GW dissipation and momentum flux decay.

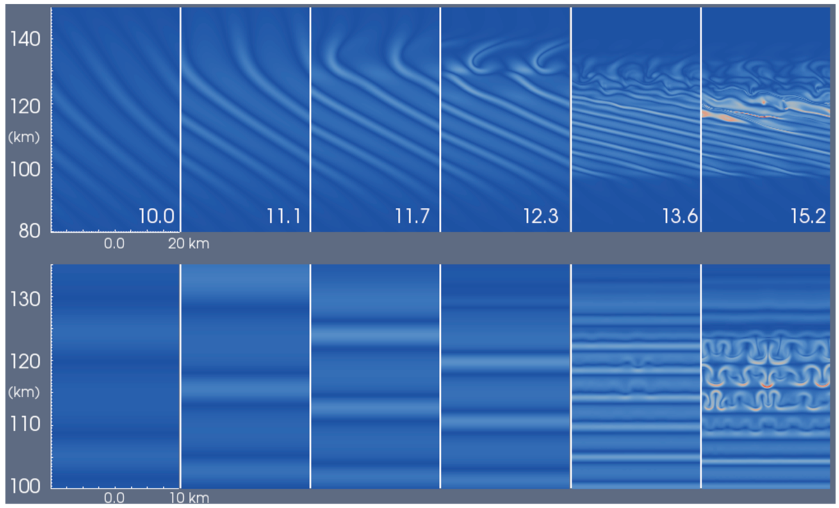

Figure 2. As in Figure 1 for Case 2. Note the accelerated and very different instability character relative to Case 1.

3.1.1. GW Phase Structures and Evolutions

Considering first the GW phase structures and their vertical evolutions, we see that Case 1 (suppressing induced mean flows) experiences intensification of positive ζ_y' relative to negative ζ_y' due to shallower parcel trajectories accompanying compressibility at larger GW amplitudes, as discussed above (see equation (8) and LF12). Case 1 exhibits very little variation in the phase structure following attainment of large amplitude and strong positive ζ_y'.

In contrast, Case 2 (allowing induced mean flows) exhibits strong phase distortion before attainment of large amplitudes and enhanced positive ζ_y' in Case 1. Phase distortions arise due to the GW occupying the fluid being accelerated or decelerated according to

$$\frac{\mathrm{d}U}{\mathrm{d}t} = -\frac{1}{\bar{\rho}}\frac{\mathrm{d}}{\mathrm{d}z}(\bar{\rho} < u'w' >) \tag{11}$$

This yields a corresponding wind profile given by

$$U(z,t) = U + \Delta U = -c - \int_0^t \frac{1}{\bar{\rho}}\frac{\mathrm{d}}{\mathrm{d}z}(\bar{\rho} < u'w' >)\mathrm{d}t \tag{12}$$

Due to the depth of the GW packet, accelerations above the $\rho_0 < u'w' >$ maximum are much larger than decelerations below. Assuming that $\rho_0 < u'w' >$ preserves the form given by equation (10) prior to strong phase distortions, initial mean flow accelerations are given approximately by

$$\frac{\mathrm{d}U}{\mathrm{d}t} \sim (z - z_0)\mathrm{e}^{z/H}\exp\left[-\frac{(z - z_0)^2}{\sigma_0^2}\right] \tag{13}$$

The result is a quadratic equation for the altitudes of maximum positive and negative accelerations, with solutions given by

$$(z - z_0) = \frac{\sigma_0^2}{4H} \pm \left(\frac{\sigma_0^2}{4H}\right)\left(1 + \frac{8H^2}{\sigma_0^2}\right)^{1/2} \tag{14}$$

For $H = 7$ km and $\sigma_0 = 20$ km (Cases 1 to 7), this yields a U minimum ~28.6 km above the $\rho_0 < u'w' >$ maximum and a maximum acceleration (deceleration) opposing U at ~34 km above (~5.8 km below) the $\rho_0 < u'w' >$ maximum (see discussion of Figure 5 below). For $H = 7$ km and $\sigma_0 = 10$ km (Cases 8 to 12), the minimum U occurs at ~7.14 km above, and the maximum acceleration (deceleration) occurs at ~11.5 km above (~4.4 km below), the $\rho_0 < u'w' >$ maximum.

The accelerations thus steepen the GW phases at the highest altitudes and reduce their slopes below, yielding a kinking of the phase near 135 km with vertical phase above at ~11.5 T_b, somewhat above the maximum of $U(z,t)$, where $\Delta U > c$ (see Figures 2–4). Strong accelerations thereafter cause a reversal of the phase slopes at higher altitudes and a stalling of the vertical progression of the GW packet. These phase distortions are

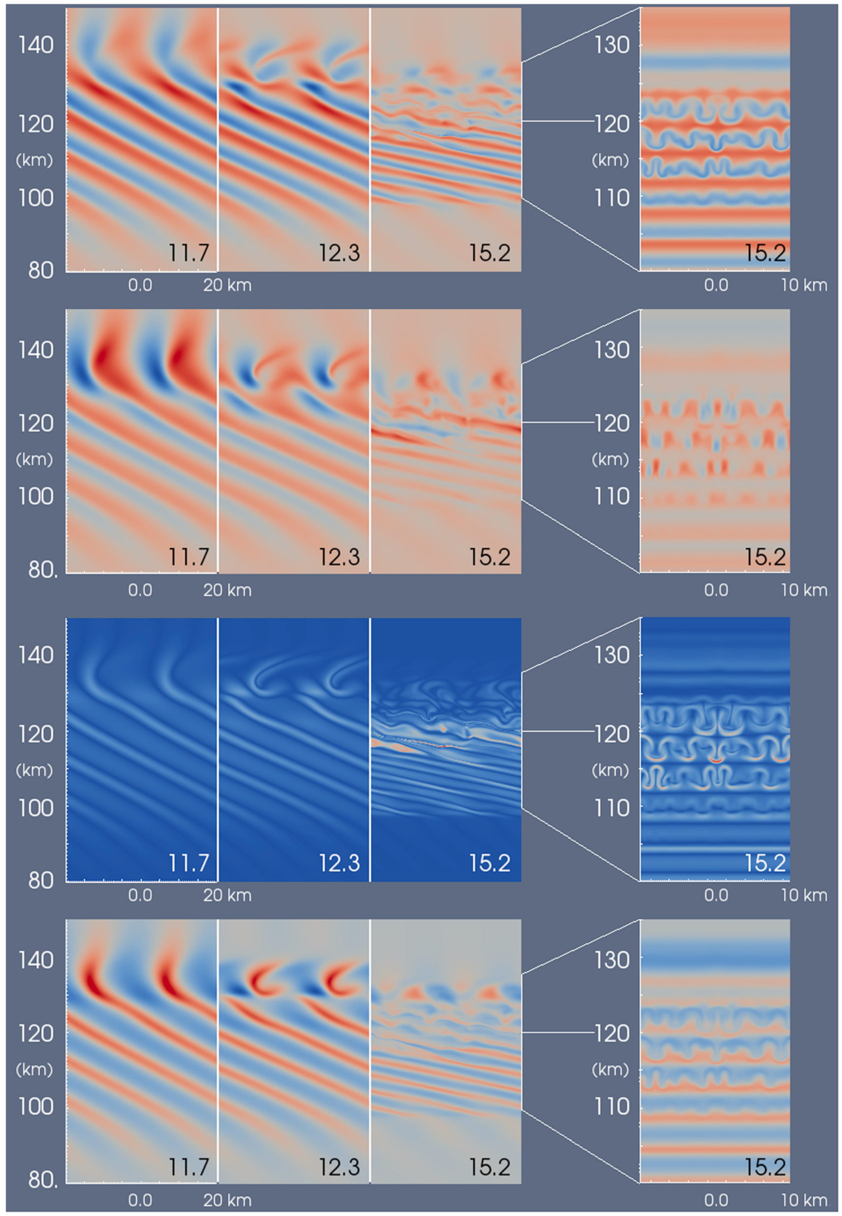

Figure 3. Streamwise cross sections of (first to third columns, top to bottom) u', w', $|\zeta_y'|$, and θ' at three times throughout the 2-D and 3-D SA instabilities in Case 2. (fourth column) Spanwise cross sections at the last time for the central portion of the vertical domain (see axis labels at the bottom left). Color scales in each vary from minimum (blue) to maximum (red) and are uniform in time for each field.

followed quickly by strong 2-D nonlinear dynamics within the GW field beginning at ~12 T_b. Importantly, these SA dynamics occur on a more rapid timescale, and at a significantly higher altitude (~10 km), than the initial nonlinear dynamics (e.g., initial roll-up of the ζ_y' sheets) in the absence of SA effects that begin at ~13.4 T_b in Case 1. They also occur at the leading edge of the GW packet, far above (by >30 km) the peak in $\rho_0<u'w'>$ at these times. As a result, SA dynamics do not initially have a strong impact on GW $\rho_0<u'w'>$, apart from decelerating the upward propagation of the central GW packet due to the induced shallower phase slopes (and reduced c_{gz}) at lower altitudes.

The evolutions of $\rho_0<u'w'>$ for Cases 1 and 2 and of $\Delta U(z)$ for Case 2 at the times shown in Figure 2 are displayed in Figure 4 (bottom and top rows). The momentum flux for Case 1 (dashed lines) extends to higher altitudes at earlier times due to its lack of SA dynamics. Case 1 also exhibits delayed instability, but at lower

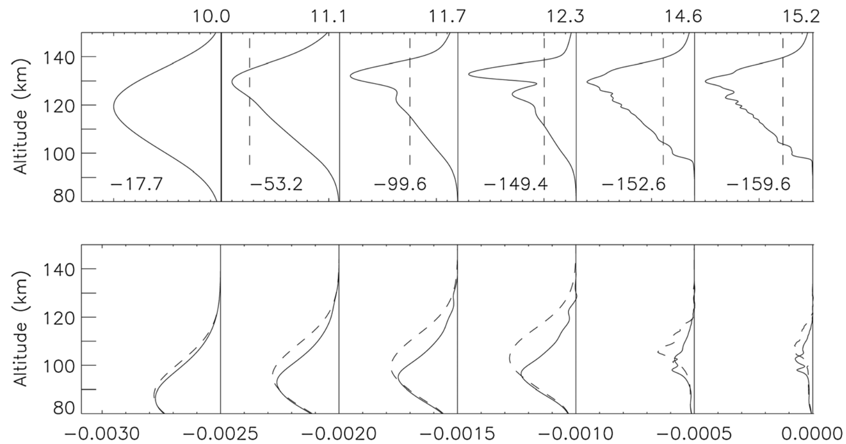

Figure 4. (top row) $\Delta U(z)$ and (bottom row) GW $\rho_0<u'w'>(z)$ profiles for Case 1 (dashed lines) and Case 2 (solid lines). Times at the top are in T_b, and the peak ΔU values at each time are shown at the bottom in Figure 4 (top row) in m s^{-1}. The $\rho_0<u'w'>(z)$ scale is shown at the bottom right in Figure 4 (bottom row) and successive profiles at smaller times are displaced by -0.005 m^2 s^{-2} to the left in each panel set. Also shown in each panel at the top is the initial GW intrinsic phase speed for reference.

altitudes, leading to momentum flux decaying at and above the altitudes of initial instability following instability onset (~13.4 T_b). This leads to momentum fluxes extending to ~135 km prior to instability but confined to decreasing altitudes as instabilities reduce the GW amplitude thereafter. In contrast, the momentum flux for Case 2 stalls earlier and lower, due to SA effects, but decays more slowly. This results in continuing decelerations at lower altitudes and accelerations at higher altitudes (along the GW propagation direction) that restore the initial $U(z)$ below ~98 km and cause the maximum ΔU to continue to increase in altitude and amplitude. By 15.2 T_b, the peak $\Delta U(z)$ has reached ~130 km, near the altitude of initial kinking of the GW phase structure and secondary 2-D instabilities. The evolution of $\Delta U(z)$ with time (Figure 4, top row) exhibits an initial profile that is approximately Gaussian prior to mean wind changes comparable to or exceeding the initial GW intrinsic phase speed ($c_i = -44$ m s^{-1}). However, induced winds become dramatic as the GW phase structure is advected through vertical at higher altitudes. In fact, ΔU increases another 100 m s^{-1} in the next ~2 T_b and approaches a value nearly 4 times larger (~160 m s^{-1}) by ~15.2 T_b. Also seen are modulations of $\Delta U(z)$ and $\rho_0<u'w'>(z)$ in altitude that become finer in time and accompany phase variations due to the progression of 2-D dynamics at these altitudes. These features are more similar to the amplitude modulations occurring at late stages of the evolution of a GW packet that is modulationally stable than to trailing modulational instabilities described by *Dosser and Sutherland* [2011], as will be seen below to accompany all SA events, and which will be discussed further in section 4.

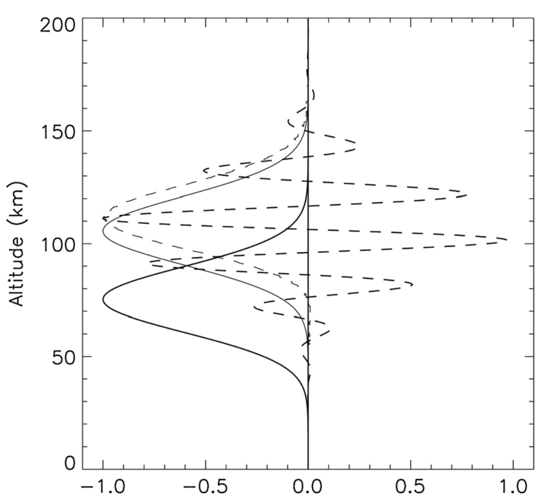

Figure 5. Profiles of $u'(z)$ (bold dashed), $\rho_0<u'w'>(z)$ (bold solid), $DU(z)$ (solid), and $dU(z)/dt$ (dashed) for the GW in Case 2 at ~4 T_b. All profiles are normalized to a maximum amplitude of 1.0.

Profiles of $u'(z)$, $\rho_0<u'w'>(z)$, $\Delta U(z)$, and $dU(z)/dt$ for the GW parameters in Case 2 are illustrated prior to the attainment of large GW amplitude in Figure 5. The packet was initially centered at 20 km, has exhibited very little dispersion propagating upward ~55 km, and has resulted in a maximum $\Delta U(z)$ ~1 m s^{-1} at the time shown in Figure 5. This $\Delta U(z)$ is much less than the initial phase speed of 44.4 m s^{-1}, so the response remains nearly linear at this stage and the functional forms given by equations (9)–(13) are still fairly accurate. These indicate that $u'(z)$, $\Delta U(z)$, and $dU(z)/dt$ all achieve their maximum responses well above the peak in $\rho_0\langle u'w'\rangle(z)$. In particular, $u'(z)$ and $\Delta U(z)$ both exhibit maxima ~30 km above, and $dU(z)/dt$ maximizes ~36 km above, that for $\rho_0\langle u'w'\rangle(z)$, in good agreement with predictions. From equation (13), we see that $dU(z)/dt = 0$ at $z = z_0$ where $d(\rho_0\langle u'w'\rangle)/dz$ changes sign. Because of the $e^{z/H}$ weighting of $\exp[-(z - z_0)^2/\sigma_0^2]$, however, accelerations along the GW propagation direction above $z = z_0$ are many times larger than decelerations below. The result is a peak in $\Delta U(z)$ that corresponds closely, but not exactly, to that in $u'(z)$, due to varying w'/u' accompanying GW propagation and phase distortions in an induced mean shear. The depth of the u' profile is also broader than $\Delta U(z)$ because $\Delta U(z)$ varies quadratically with GW velocities, both of which are roughly Gaussian prior to strong phase kinking.

3.1.2. GW Instabilities

Turning to the instabilities accompanying Cases 1 and 2, we see that the positive ζ_y' intensification noted above in Case 1 (Figure 1, suppressing induced mean flows) enables roll-up of the positive ζ_y' sheets that commences at ~13.4 T_b and exhibits immediate 3-D character (with spanwise variations and implied ζ_x' and $\zeta_z' \neq 0$) and rapid intensification thereafter. The successive evolution closely follows that described by LF12 and leads to large-scale 3-D turbulence at later stages (not shown here).

Instabilities in Case 2 depart significantly from those in Case 1. Case 2 exhibits positive ζ_y' enhancements at early stages, but these fail to become as intense as in Case 1. Nonlinear dynamics accompanying the sharp phase kink and phase reversal seen at ~130 km and ~11 T_b and after (Figure 2) yield a cascade to smaller scales in the $|\zeta_y'|$ field that remain entirely 2-D (no spanwise variations, e.g., $\zeta_x' = \zeta_z' = 0$) above ~130 km throughout the time series displayed. However, 3-D instabilities (with ζ_x' and $\zeta_z' \neq 0$) are seen to arise following the initial 2-D instabilities in the strongly sheared GW phase structure at ~110 to 130 km.

Three-dimensional instabilities at lower altitudes arise due to strong GW shears in regions that are also convectively unstable. These correspond closely to similar instabilities seen in convectively unstable sheared boundary layers, the outer braided structures in Kelvin-Helmholtz billows at high *Re* and small Richardson numbers, $Ri = N^2/(dU/dz)^2 \ll 0.25$, and similar environments arising due to superpositions of GWs and mean flow fine structure shears [*Fritts et al.*, 2013]. In each case, the instabilities comprise counterrotating streamwise-aligned rolls, yielding the distorted $|\zeta_y'|$ structures seen at 15.2 T_b in Figure 2 (bottom row, sixth column). These instabilities have spanwise scales that depend on the local *Re* ($= c\lambda_z/\nu = \lambda_z^2/\nu T_b$) and thus increase with altitude where λ_z and T_b are relatively uniform, as seen in Figure 2.

3.1.3. GW Dissipation and Momentum Flux Decay

GW dissipation in Case 1 accompanies the formation of 3-D instabilities and their cascade of energy to smaller scales, as described for similar dynamics discussed previously by LF12. Dissipation is initiated at ~120 km and expands to altitudes of ~110 to 130 km within ~0.3 T_b (see Figure 1). This energy cascade reduces the GW amplitude and momentum flux significantly but does not destroy the GW altogether. By ~15.2 T_b, however, it has reduced the GW amplitude by ~50 to 70% and reduced $\rho_0\langle u'w'\rangle$ of the packet by ~80 to 90% (Figure 4).

Initial GW instabilities in Case 2 occur more quickly than in Case 1, as discussed above. The rapid evolution of the initial 2-D SA instability and its disruption of the GW vertical propagation induce more rapid momentum flux reductions than in Case 1 at higher altitudes. The induced $\Delta U(z)$ also impose a reduced c_i and λ_z (hence also a smaller c_{gz}, as noted above) that delays the vertical propagation of the trailing portion of the GW packet (see Figure 4, bottom row, from 11.1 to 12.3 T_b). The trailing GW packet momentum flux remains nearly constant at these times, however, because of the delayed 3-D instabilities at these altitudes. Once the 3-D instabilities arise, the momentum flux decays quickly thereafter.

3.2. Effects of Varying GW Amplitude, Wavelength, Packet Depth, and Frequency

3.2.1. GW Amplitude Effects

We anticipate that any GW packet having the same initial parameters and environment, except for amplitude (or alternatively the altitude of excitation), will exhibit identical propagation and dynamics, apart from the influences of differing *Re*. To explore these influences, two DNS of GWs having the same parameters as Case 2, but initiated with a 30 times larger amplitude at altitudes differing by 50 km, were also performed (designated Cases 3 and 4 having $z_0 = 60$ and 10 km, respectively). Results of these DNS are compared using streamwise cross sections of $|\zeta_y'|$ at the same times in Figure 6. Results are displayed at much earlier times than in Case 2 because of the much larger initial amplitudes, hence smaller propagation depths needed to achieve

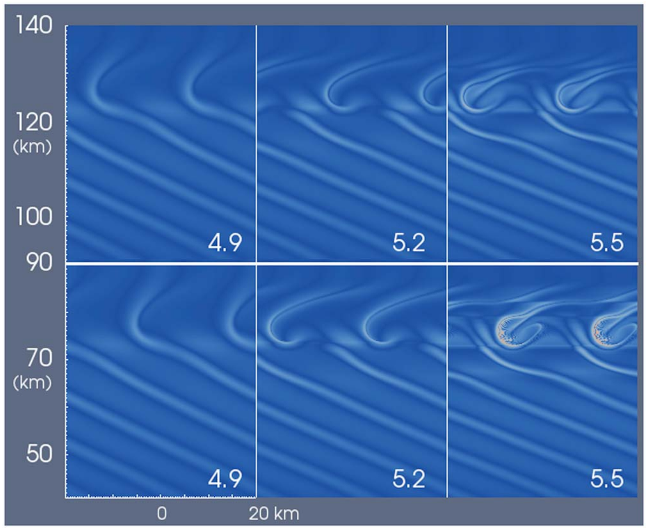

Figure 6. As in Figure 2 (top row) for (top row) Case 3 and (bottom row) Case 4. Times are at the bottom right in each panel.

SA dynamics. Times displayed span 0.6 T_b from initial strong kinking of the GW phase structures to the last stages of the 2-D evolution preceding 3-D instabilities. The two cases yield nearly indistinguishable $|\zeta_y'|$ fields at 4.9 and 5.2 T_b. Only at 5.5 T_b are there clear differences due to larger $|\zeta_y'|$ at smaller scales enabled by the larger *Re* (by $>10^3$) at lower altitudes. Even here, the dynamics are very similar but apparently slightly delayed at the higher altitudes and lower *Re* due to the weaker $|\zeta_y'|$ and smaller implied advection velocities. The implication is that SA dynamics are essentially the same over a large range of *Re*.

3.2.2. GW Wavelength Effects

Influences of varying GW wavelength on SA dynamics are illustrated with streamwise cross sections of u' and $|\zeta_y'|$ at comparable stages in the evolutions in Figure 7 (top and bottom rows). Three cases having GW $\lambda_x = 10$, 20, and 40 km are displayed (see Cases 5–7 in Table 1). Apart from the obvious differences in GW amplitudes and spatial scales, GW parameters are as similar as possible in each case. These include common initial wavelength ratios, packet depths, initial intrinsic frequencies, and comparable ratios of GW amplitudes to intrinsic phase speeds: e.g., common $\lambda_{x0}/\lambda_{z0}$, σ_0, $\omega_{i0} = N/1.43$, and $u_0'/(c - U)$. Times required to achieve comparable SA dynamics vary strongly, however, due to vertical group velocities that vary roughly as vertical wavelengths.

The SA dynamics for varying wavelengths exhibit both strong similarities and clear differences. Similarities between the three cases include the following: (S1) strong kinking of the GW phase structures exhibiting a phase reversal above the peak phase advection having a depth of ~λ_{z0}, (S2) refraction of the trailing GW phase structures to $\lambda_z < \lambda_{z0}$, (S3) intensification of the positive ζ_y' sheets and their 2-D roll-up at the lower edge of the region of peak advection, and (S4) similar time scales for the nonlinear SA dynamics following reversal of the phase structure at higher altitudes.

Differences between the three cases include the following: (D1) stronger positive ζ_y' enhancements for larger initial GW scales; (D2) more intense vorticity dynamics for larger initial GW scales; (D3) SA dynamics occurring at smaller relative, but larger spatial, scales for the larger GWs; (D4) increasing altitudes of the peak advection

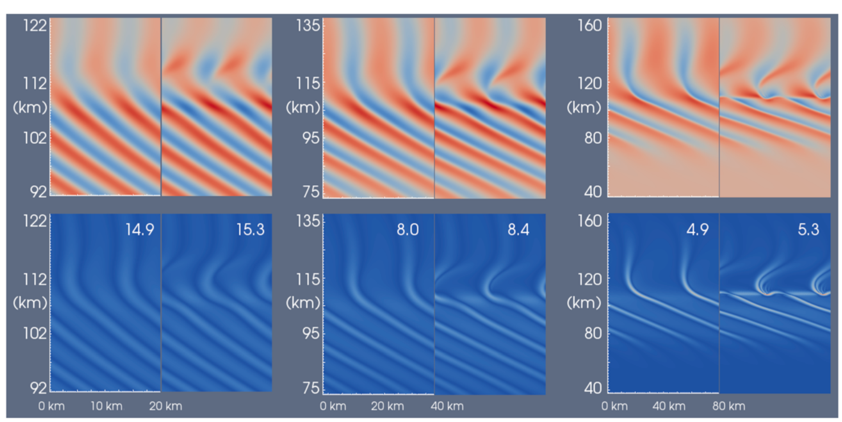

Figure 7. As in Figure 3 showing streamwise cross sections of (top row) u' and (bottom row) $|\zeta_y'|$ for (left to right) Cases 5 to 7. Times are at the top right in Figure 7 (bottom row).

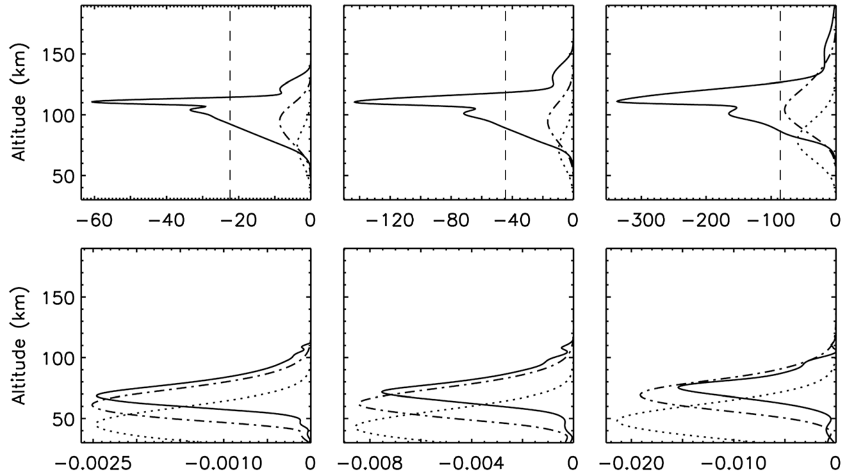

Figure 8. Profiles of (top row) $\Delta U(z)$ and (bottom row) $\rho_0 < u'w' > (z)$ for (left to right) Cases 5 to 7. Times are 7.2, 12.2, and 15.2 T_b (Case 5); 3.4, 6.4, and 8.4 T_b (Case 6); and 2.3, 4.3, and 5.3 T_b (Case 7). Lines in each case are dotted, dash-dotted, and solid, respectively, from earlier to later times. The first mean wind profile is shown at 5, 10, and 20 times their true amplitude for Cases 5–7, respectively. The initial GW intrinsic phase speeds are shown in each panel at the top with a vertical dashed line.

with increasing GW wavelengths for common GW source altitudes, packet depths, and $u_0'/(c-U)$; and (D5) larger λ_z decreases at altitudes below the region of maximum SA for larger GW scales.

Similarities between the SA dynamics accompanying the three different GW scales in Cases 5–7 are not surprising, given the discussion of these SA dynamics for Case 2. Specifically, the phase kinking and refraction (S1 and S2) arise from the form of equation (12) for $\rho_0 < u'w' >$ given by equation (10). Likewise, S3 arises from the more shallow parcel orbits than the corresponding GW phases in all cases due to finite $\varepsilon = \lambda_z/4\pi H$ in equation (8). Similar time scales of SA dynamics (S4) occur because GW amplitudes, u', leading to SA dynamics are proportional to the GW intrinsic horizontal phase speed, $(c-U)$ (or λ_z), and the GWs in Cases 5–7 experienced the same relative growth between their sources and SA dynamics altitudes.

Differences in the SA dynamics noted above can also be traced to specific causes in most cases. Stronger positive ζ_y' enhancements occur for larger GW scales due to shallower parcel orbits for larger λ_z; see equation (8). While initial SA dynamics are similar among Cases 5–7, more intense vorticity dynamics are observed at comparable stages for larger λ_z due to larger Re (varying as λ_z^2) and correspondingly larger $|\zeta_y'|$ and stronger interaction dynamics. Sharper gradients accompanying larger Re also enable smaller-scale instability structures to arise compared to the GW scales.

Momentum flux and $\Delta U(z)$ profiles at 3 times for Cases 5–7 are shown in Figure 8 (bottom and top rows). Times shown span 8, 5, and 3 T_b for the three cases because of the higher c_{gz} for larger λ_z, and the final profiles in each case correspond to the final times shown in Figure 7. Momentum flux maxima and distribution depths both decrease between the last two times in each case, implying that SA dynamics are having strong influences at these times. This can also be inferred from the stages of the SA instabilities in Figure 7 or by comparing $\Delta U(z)$ and the initial c_i in each case, the ratios of which increase from ~0.4 to ~0.9 with increasing initial c_i and λ_z.

At the final times shown in each case, the $\Delta U(z)$ profiles are quite similar, but are somewhat higher and broader for the larger initial GW scales, despite the same initial packet depths for the three cases. Possible causes for these differences include (1) more rapid vertical dispersion for the larger GW scales having smaller ratios of σ_0/λ_z, (2) broader SA dynamics occurring for larger λ_z, and/or (3) more vigorous SA dynamics at larger λ_z and higher Re.

3.2.3. GW Packet Depth Effects

Effects of different GW packet depths are illustrated with Case 5 discussed above and Case 8 differing only in having a packet depth 2 times smaller than in Case 5. Streamwise cross sections of u' and $|\zeta_y'|$ (top and bottom rows) are shown at comparable stages in the SA dynamics for Cases 5 and 8 at left and right, respectively, in Figure 9. Corresponding induced $\Delta U(z)$ and GW $\rho_0 < u'w' > (z)$ profiles are shown at 3 times in Figure 10. SA dynamics in these cases agree fairly closely, apart from the ~18 km lower SA responses for the shallower

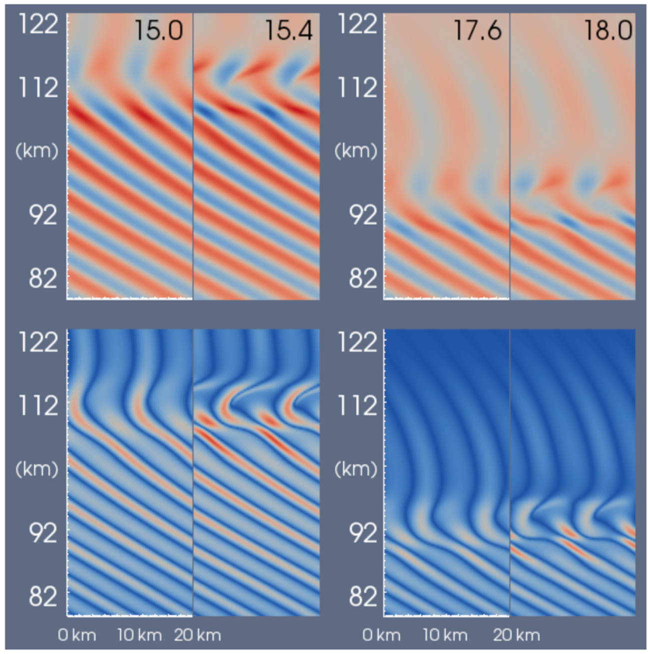

Figure 9. As in Figure 7 for the comparison of (left column) Case 5 and (right column) Case 8. Times are at the top right in Figure 9 (top row).

GW packet. Importantly, the major result, a large difference in the altitude of primary SA effects, is largely consistent with that predicted by equation (14), e.g., a difference in the altitudes of major implied accelerations between the two cases of ~18 km, with the lower altitude effects expected for the smaller Case 8 $\sigma_0 = 10$ km, as observed.

This result may seem contradictory, given the larger responses of the wider GW packet at higher altitudes, with larger GW perturbations and implied mean flow accelerations. What is most important for GW SA dynamics are the induced mean wind shears, and these are dictated by both the GW momentum flux at the leading edge and the packet depth (stronger induced shears for a narrower packet). Note that the u' fields in Figure 9 have the same color scale. Indeed, the u' amplitudes for the narrower packet at right are almost exactly $2^{1/2}$ smaller, thus a momentum flux ~2 times smaller. Together with gradients that are 2 times larger, this accounts for the SA dynamics occurring at lower altitudes for the narrower and "weaker" GW packet.

Remarkably, despite the very different altitudes relative to the GW momentum fluxes and *Re*, very similar features are seen in the u' and $|\zeta_y'|$ fields above and below the region of strong phase kinking. These include similar SA kinking behavior, with stronger kinking and roll-up of the positive spanwise vorticity phases, local intensification and modulation of the negative spanwise vorticity phases, and very similar phase structures and wavelengths above and below the region of strong SA responses. The detailed structures in the $|\zeta_y'|$ fields also reveal clear differences, however. The most prominent are larger phase shifts occurring over a shorter interval above the maximum phase kinking for the deeper GW packet, with more pronounced and horizontally elongated regions of enhanced ζ_y' of both signs.

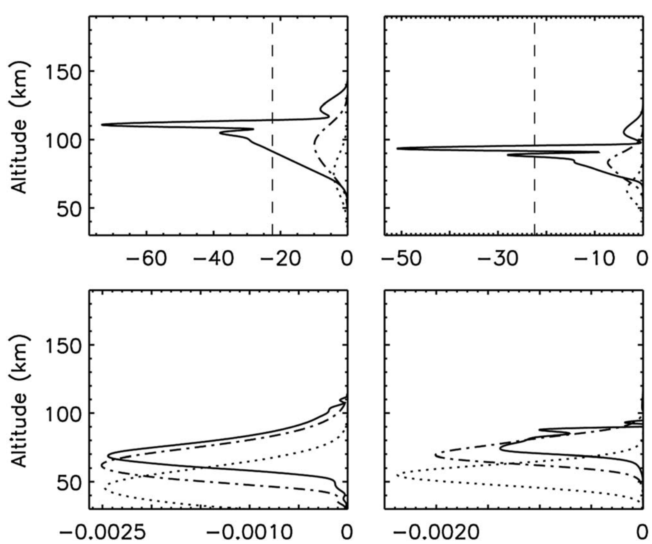

Figure 10. As in Figure 8 but for (left column) Case 5 and (right column) Case 8. Times are 7.4, 12.4, and 15.4 T_b (Case 5) and 10.1, 15.1, and 18.1T_b (Case 8). Line codes are as in Figure 8. The earlier mean wind profiles in each case are shown at 5 times their true amplitude.

These differences are surely influenced by the differing vertical profiles of the mean flow accelerations implied by equation (13). Stronger shears are implied by the narrower Gaussian dependence in Case 8. However, there is no evidence of stronger shearing in the vorticity fields near the altitude of maximum kinking in Case 8 relative to Case 5 in Figure 9, especially given the longer interval displayed for Case 8. Different *Re* are also unable to account for these differences, given that *Re* is >10 times smaller for the SA event at higher altitudes in Case 5 compared to Case 8, but Case 5 exhibits sharper features. Thus, there must be other factors

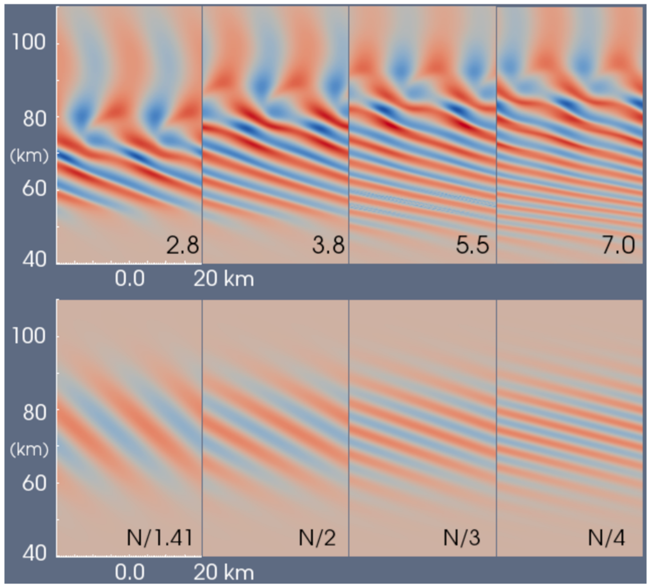

Figure 11. As in Figure 3 showing streamwise cross sections of u' for (left to right) Cases 9 to 12 at (bottom row) the initial time and (top row) 2.8, 3.8, 5.5, and 7.0 T_b for which the four cases exhibit very similar SA phase structures and dynamics.

that also influence these dynamics and profiles at the altitudes exhibiting the largest SA effects.

Profiles of $\Delta U(z)$ and GW $\rho_0\langle u'w'\rangle(z)$ spanning 8 T_b for Cases 5 and 8 are shown in Figure 10. The two $\Delta U(z)$ responses are very similar in form, each having a strong primary maximum, a secondary peak of approximately one half the primary maximum ~5–7 km below, and a tertiary peak of approximately one tenth the primary maximum ~12–15 km above. The $\rho_0\langle u'w'\rangle(z)$ profiles exhibit a similar initial evolution in altitude, with each peak moving upward ~15 km over 5 T_b but with differences in the rate of evolution and leading edge form at higher altitudes thereafter. This is likely due, in part, to the stronger gradients and more rapid SA evolution within the final 0.4 T_b accompanying the SA dynamics for Case 8 (see the stronger phase distortions for Case 8 in Figure 9, right column). However, each momentum flux evolution exhibits similar leading edge fluctuations at later stages, so Case 8 is also slightly further advanced at the times shown. Additional DNS not shown reveal that these features are relatively insensitive to GW amplitude.

3.2.4. GW Frequency Effects

Influences of varying initial GW intrinsic frequency, ω_{i0}, on SA dynamics are shown with streamwise cross sections of u' at initiation and at comparable stages in the nonlinear SA dynamics at later times in Figure 11 (bottom and top rows, respectively). Shown are results for $\omega_{i0} = N/1.43$, $N/2$, $N/3$, and $N/4$, with other parameters as listed for Cases 9 to 12 in Table 1. Note that u' is nearly the same in each case, causing the initial $\rho_0\langle u'w'\rangle$ to vary approximately as ω_{i0}/N; see equation (8). Profiles of $\Delta U(z)$ and $\rho_0\langle u'w'\rangle(z)$ at initiation and at an intermediate and late time for each case are displayed in Figure 12.

As seen for Cases 5–7 above, we see both strong similarities and interesting differences among the SA dynamics in Cases 9 to 12. Similarities include the following: (S1) nearly indistinguishable responses in GW and 2-D instability phase structures near the maxima of SA dynamics and above; (S2) nearly identical λ_z immediately below the regions of strong SA dynamics in each case, despite their very different λ_{z0}; (S3) comparable maximum $\Delta U(z)$ at the altitudes of SA dynamics (within ~30%), despite the very different initial intrinsic phase speeds, c_{i0}, (and λ_{z0}) in the four cases; and (S4) momentum fluxes at late stages in each cases that exhibit greater structure above the maximum than seen for the deeper GW packets considered above.

Differences among the SA dynamics for Cases 9 to 12 displayed in Figures 11 and 12 include the following: (D1) delayed SA responses at higher altitudes for the smaller initial GW intrinsic frequencies due to their smaller vertical group velocities; (D2) very different degrees of λ_z compression at ~10–20 km below the region of SA dynamics, with $\lambda_z \sim \lambda_{z0}$ for $\omega_i = N/4$ and compression by ~2 times for $\omega_{i0} = N/1.43$; (D3) different altitudes at which SA dynamics occur, e.g., higher for lower ω_{i0}, because of the reduction in $\rho_0\langle u'w'\rangle$ and higher attainment of SA effects for fixed u' and σ_0; (D4) quite different $\Delta U(z)$ profiles for the different ω_{i0}, e.g., much narrower responses similar to earlier cases with larger σ_0 for larger ω_{i0}, but much broader distributions in altitude having greater structure below the maximum for smaller ω_{i0}; and (D5) weaker, more extended $\rho_0\langle u'w'\rangle(z)$, but with higher variability, for smaller ω_{i0} above the maxima at the later times exhibiting significant SA dynamics.

Similarities in SA dynamics seen in Figure 11 (where λ_{z0} and ω_{i0} vary by factors of ~3) can be traced to vertical variations of $\Delta U(z)$ implied by equation (13). These suggest similar vertical scales of SA dynamics

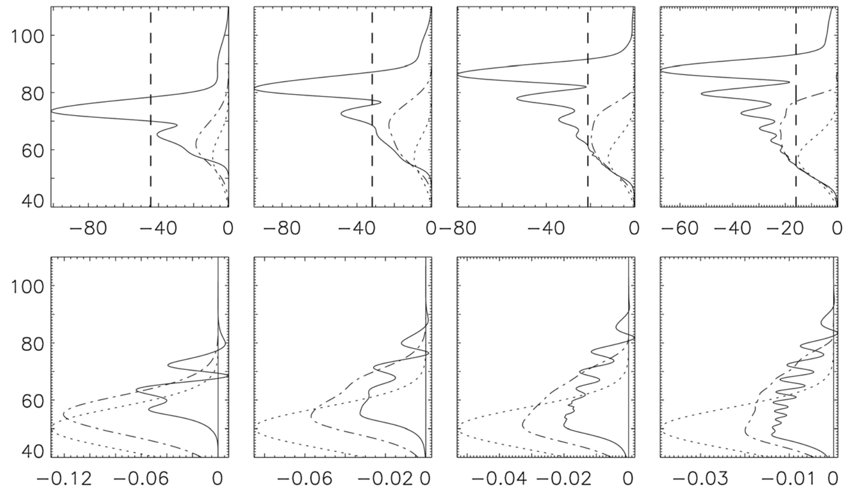

Figure 12. As in Figure 8 for Cases 9 to 12. Times are 0, 0.8, and 2.8 T_b (Case 9); 0, 1.8, and 3.8 T_b (Case 10); 0, 2.5, and 5.5 T_b (Case 11); and 0, 4, and 7 T_b (Case 12). Line codes are as in Figures 8 and 10.

for common σ_0, as observed in the discussion of wavelength effects, independent of other GW parameters. The different altitudes of SA instability are consistent with the different initial $\rho_0 \langle u'w' \rangle$, suggesting that to lowest order, it is only the initial $\rho_0 \langle u'w' \rangle$ that determines the altitude of primary SA dynamics for common σ_0. The more significant differences in the cases illustrated in Figure 12 arise due to the GWs in Cases 11 and 12 requiring greater depths over which to yield strong SA dynamics (due to their smaller $\rho_0 \langle u'w' \rangle$) and having smaller vertical group velocities, compared to Cases 9 and 10. Together, these influences appear to impose smaller gradients in $\rho_0 \langle u'w' \rangle$ as ω_{i0} increases that more closely resemble those for Case 2 shown in Figure 4. Together with the results of other cases discussed above, these results suggest considerable universality in the SA dynamics accompanying transient GW packets that are localized only in altitude and time.

3.3. Multiple GW SA Events

The cases discussed above, and equations (11)–(14), indicate that SA dynamics are largely driven by the $\rho_0 \langle u'w' \rangle$ gradients at the leading edges of GW packets based on the $\rho_0 \langle u'w' \rangle$ profile. In each case, a small portion of the GW packet that occurs above the altitudes of primary SA effects continues to propagate to higher altitudes. This can be seen clearly in Figure 5, which shows that the peak GW u' is only slightly below

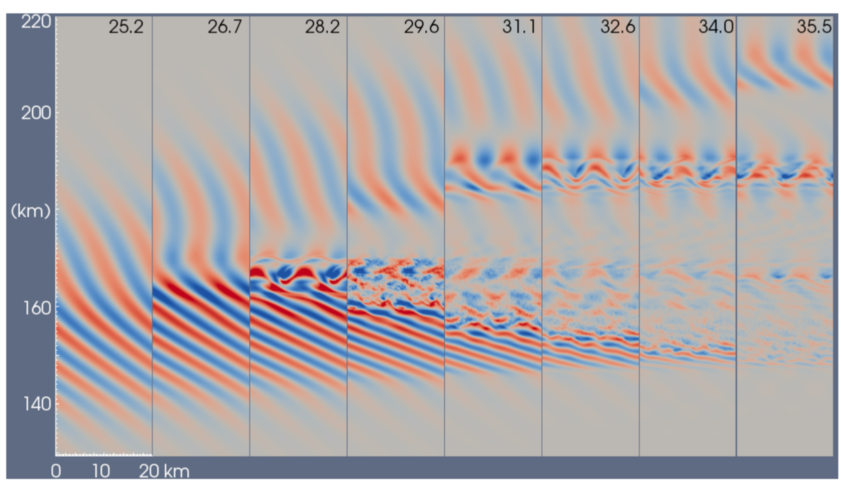

Figure 13. As in Figure 11 for Case 13 from 25.2 to 35.5 T_b. Note the occurrence of three altitudes exhibiting SA dynamics at ~3 T_b intervals and displaced upward by ~20 km in each case. SA dynamics become less vigorous with increasing altitude because Re decreases by ~17.4 in each successive event.

the maximum $\Delta U(z)$ and that u' has fallen by <50% where $\rho_0\langle u'w'\rangle$ appears to approach zero. This suggests the potential for SA dynamics to again accompany the surviving GW packet as it increases in amplitude at higher altitudes. Figure 13 shows this to be the case. Indeed, successive SA events follow the first, each at an altitude ~20 km higher that the previous event. This implies that each event evolves from an initial $\rho_0\langle u'w'\rangle$ that is ~17.4 times smaller than what triggered the previous event. For the first event, this is ~8 times smaller that the peak initial $\rho_0\langle u'w'\rangle$.

Successive events also appear to be similar in form initially but differ strongly in their primary and secondary instabilities because of the ~17.4 times reduction in *Re* accompanying each successive event. Indeed, only the first event exhibits strong primary 2-D and secondary 3-D instabilities. The second event exhibits clear primary 2-D instability, while the third event shows strong phase kinking and indications of 2-D instability that occurs, but more weakly, at later times than shown in Figure 13. The first event has $Re = \lambda_z^2/\nu T_b \sim 1$ because of the very large $\nu \sim 3 \times 10^5$ at ~166 km (for our assumed isothermal temperature profile). The successively higher events have *Re* ~0.06 and 0.003, respectively. These results suggest that SA dynamics should be ubiquitous throughout the atmosphere wherever deep vertical propagation and sufficiently large *Re* allow GWs to achieve large amplitudes and induced local mean flows.

4. Summary, Discussion, and Conclusions

Our results have demonstrated the effects of GW self-acceleration (SA) for a range of GW amplitudes, wavelengths, intrinsic frequencies, and packet depths in initially uniform mean wind and temperature fields. These considerably generalize earlier results for a Boussinesq fluid by *Sutherland* [1999, 2006a] and for an anelastic atmosphere by *Dosser and Sutherland* [2011] and *Fritts and Lund* [2011]. Results described here employ GW packets that are localized only in the vertical and time and have initial Gaussian distributions of momentum flux in altitude of infinitesimal magnitude. As a GW packet propagates to higher altitudes, it transports a momentum deficit, and an implied mean wind change, $\Delta U(z)$, that increases as $1/\rho$ and largely accompanies its leading edge, because of the exponentially smaller mean density at higher altitudes; see equations (11)–(13). As examples, the maximum mean flow decelerations occur higher than the maximum momentum fluxes by ~11.5 and 34 km for GW Gaussian momentum flux standard deviations of $\sigma_0 = 10$ and 20 km for $H = 7$ km. Similarly, the maximum $\Delta U(z)$ occurs higher than the maximum momentum fluxes by ~7.14 and 28.6 km, respectively.

The leading edge mean flow decelerations have two effects on a GW packet as they increase in magnitude. First, at altitudes experiencing strong decelerations, the leading edge of the GW packet is "self-accelerated" in the direction of GW propagation (opposite to the decreasing mean wind) because it resides in the flow being decelerated. Because GW SA is localized in altitude, this causes strong kinking of the leading edge phase structure and cessation of vertical propagation where the phase becomes uniform in altitude and $c_{gz} = 0$. These effects occur roughly as the induced mean flow exceeds the initial GW phase speed. A second response to the mean flow decelerations is decreasing c_i and refraction to smaller λ_z of the trailing GW packet where it encounters decreasing mean winds, yielding decreasing intrinsic phase speeds. Mean flow decelerations continue, however, because no GW dissipation and momentum flux reductions have yet occurred and momentum flux gradients remain large.

GW dissipation thereafter is driven by both 2-D and 3-D instability dynamics as the various SA dynamics become strong. The first instability to occur in all cases is a 2-D SA instability. This occurs at the leading edge of a GW packet beginning with the initial phase distortions and evolving to include phase kinking, overturning, and a cascade to smaller horizontal and vertical scales that remain 2-D for an extended interval. This is followed by 3-D instability of the trailing GW phases at lower altitudes that have evolved to smaller λ_z and large (locally overturning) amplitudes. Three-dimensional instabilities comprise streamwise-aligned (along the GW propagation direction), counterrotating vortices (with largely spanwise wave numbers) similar to the secondary instabilities in the outer portions of Kelvin-Helmholtz billows and in initial multiscale GW and mean shear superpositions [e.g., *Fritts et al.*, 2013]. The accompanying GW dissipation confines the momentum flux divergence and mean flow accelerations to lower altitudes than occur in the absence of SA effects, as noted by *Scinocca and Sutherland* [2010] and *Dosser and Sutherland* [2011] and seen in Figure 4.

Our various cases have revealed SA dynamics to be surprisingly robust and similar for different GW spatial and temporal scales, packet depths, and *Re*. Larger GW scales lead to more rapid SA dynamics because of larger c_{gz} and to more rapid 2-D instability evolutions due to the much enhanced positive ζ_y (see Figure 7). The vertical scales of SA dynamics are also remarkably similar for GWs having very disparate λ_{z0} and ω_{i0}, and *Re*, but common packet depths. The major differences arise in the $\rho_0 \langle u'w' \rangle$ and ΔU profile evolutions that occur for different ω_{i0} accompanying GW propagation and dissipation, and the modulations of these profiles as the GW packets exhibit SA dynamics. The modulations differ significantly because the scales of variability correspond to the GW vertical wavelengths, which are similar near the initial SA altitude but are much smaller at lower altitudes for the smaller ω_{i0}.

Compression of the GW $\rho_0 \langle u'w' \rangle$ and ΔU profiles in the vertical occurs for $\omega_{i0} \sim N/2^{1/2}$, except for Cases 8 and 9. Case 8 has $\lambda_{z0} = \lambda_x = \sigma_0 = 10$ km, which imply smaller c_{gz} and σ_0 and allow greater dispersion than the other cases having $\omega_{i0} \sim N/2^{1/2}$ that propagate over significant altitudes. Case 9 exhibits only minor compression because it has a large initial amplitude and very quickly exhibits SA instability. The compression in Cases 2–7, rather than expansion due to dispersion anticipated by the anelastic results of *Dosser and Sutherland* [2011], cannot be due to modulational instability because the initial $\lambda_{z0}/\lambda_x \sim 1$ for these cases are much smaller than the modulational instability threshold of $\lambda_{z0}/\lambda_x = 2^{1/2}[1 + \lambda_x^2/(4\pi H)^2]^{-1/2}$. These differences must instead be attributed to the different initial conditions, which include deeper packets by ~2.2–4.4 times and smaller initial GW amplitudes than employed by *Dosser and Sutherland* [2011], implying greater amplitude growth and eventual nonlinearity that offsets much weaker dispersion in the results here. Additional evidence against modulational instability in Cases 2–7 are the altitudes at which SA dynamics occur, which are all much higher than z_{break} for these cases (see Table 1).

In contrast, Cases 10–12 having $\omega_{i0} = N/4$ to $N/2$ exhibit expansion of the $\rho_0 \langle u'w' \rangle$ and ΔU profiles with increasing time and altitude. These tendencies are consistent with the packet expansion predicted to accompany modulational stability for Boussinesq and anelastic fluids by [*Sutherland*, 2006a] and *Dosser and Sutherland* [2011]. These GW packets also readily propagate to altitudes above z_{break}, as anticipated by the weakly nonlinear theory (see Table 1).

Profiles of ΔU and $\rho_0 \langle u'w' \rangle$ accompanying initial SA instabilities evolve significant variations in the vertical for all λ_{z0}, ω_{i0}, and σ_0 considered. For the GW packets having $\omega_{i0} = N/4$ and $N/3$ (Cases 11 and 12; see Figure 12, third and fourth columns), the modulations resemble those found by *Dosser and Sutherland* [2011] for $\lambda_{z0} = 0.7\lambda_x$ if we infer GW vertical displacements $\xi'(z)$ from our $\rho_0 \langle u'w' \rangle(z)$. These exhibit a leading peak followed by successive smaller peaks at smaller vertical spacing on a decreasing mean with decreasing altitude. Case 9 and Case 10 ($\omega_{i0} = N/1.4$ and $N/2$) profiles exhibit fewer maxima and much less expansion of the packets in the vertical. In all cases, the smaller positive values of $\rho_0 \langle u'w' \rangle$ near the leading edges of the packets imply partial reflection in these regions due to kinking of the phase structure that causes c_{gz} reversal.

Other profiles of ΔU and $\rho_0 \langle u'w' \rangle$ for $\omega_{i0} = N/1.4$ at late times differ significantly from those obtained for $\omega_{i0} = N/4$ to $N/2$, despite predictions of modulational stability for $\lambda_{z0} = \lambda_x$. Specifically, Cases 5–8 have ΔU profiles that more closely resemble those for the case of modulational instability of *Dosser and Sutherland* [2011], though they also exhibit SA instability above the altitude predicted for linear overturning. These responses arise because of the deep propagation and very large GW amplitude increases enabled by their very small initial amplitudes. The exceptions are Case 2, which had a very small initial amplitude (5 times smaller than Case 6) and thus exhibited linear dispersion and SA dynamics at much higher altitudes, and Case 9, which exhibited SA dynamics almost immediately without packet compression.

Finally, to evaluate the accuracy of our anelastic solutions for the evolving GWs and induced mean flows, we compare the induced mean momentum and mean winds for Case 2 with those predicted by conservation of pseudomomentum [*Rieper et al.*, 2013]. GW action and pseudomomentum were calculated from the GW perturbations and phase variations with altitude at 10.5, 11, and 11.5 T_b (at which the GW phase slope approaches vertical). Generally very good agreement was found, given the uncertainties in these estimates. Pseudomomentum estimates of mean momentum and mean wind maxima increase from ~1% at 10.5 T_b to ~2–4% at 11.5 T_b, relative to the direct FV code fields. Pseudomomentum estimates also imply slightly faster vertical GW dispersion at the leading edge, yielding $U(z)$ maxima and widths that are ~1 km higher (relative to a ~100 km propagation depth) than the direct FV code profiles. Small differences also occur in the vertical structures of the induced mean winds at 11 and 11.5 T_b. However, these differences appear to be relatively insignificant, given the uncertainties in the initial GW and mean wind specifications. The implications are that the FV code performs well, even in cases where density perturbations push the limits of the anelastic approximation. For reference, the ρ'/ρ maxima are -0.11 and 0.19 at the maximum SA altitude (~130 km), with the narrower, stronger positive excursion due to the asymmetry in the velocity field noted above.

SA dynamics described here appear inevitable for most GW packets that achieve large amplitudes, at least in the absence of large mean wind shears and/or large variations in N^2, which cause additional dynamical effects. This is because the majority of energy and momentum fluxes is associated with GWs that have λ_z/λ_x significantly less than the threshold for modulational instability. For these GWs, mean wind shears that increase (decrease) c_i, λ_z, and c_{gz} as a GW propagates upward will cause the altitude of SA dynamics to increase (decrease) by extending (shortening) the leading edge of the GW momentum flux distribution; e.g., an increased leading edge σ significantly increases penetration to higher altitudes prior to strong SA dynamics (see Figure 9). Larger wind shears or N^2 increases that decrease c_i, λ_z, and/or c_{gz} will strongly restrict SA dynamics, especially as a critical level is approached. This is more likely for GWs having smaller initial c_i, λ_z, and c_{gz}. Conversely, wind shears or N^2 decreases that increase c_i, λ_z, and/or c_{gz} will allow SA dynamics to extend to higher altitudes, at least for GWs having λ_z/λ_x that remain below the threshold for modulational instability and avoid turning levels. However, *Sutherland* [1999] has noted the potential for large-amplitude GW packets to penetrate to altitudes above a turning level under suitable conditions; hence, additional studies are needed to evaluate these dynamics in such environments.

While our results are for GW packets localized only in altitude and time, initial simulations of 2-D and 3-D localized GW packets suggest similar dynamics because the horizontal scales of a GW packet typically exceed the vertical scales on which SA dynamics occur. This implies that the local mean flow variations will still be a significant fraction of those obtained for a GW packet localized only in the vertical. These additional studies of SA dynamics for 2-D and 3-D localized GW packets will be reported elsewhere.

SA dynamics also have important implications for general modeling of GW dynamics and effects in the MLT and perhaps at lower altitudes [e.g., *Scinocca and Sutherland*, 2010]. The rapid vertical propagation and large-amplitude increases occurring for deep GWs virtually guarantee strong mean flow interactions, instabilities, and local body forcing where amplitudes become large. These dynamics in turn impose major changes (1) in GW character, spatial scales, amplitudes, and momentum fluxes; (2) in the local mean flow in 1-D, 2-D, or 3-D, depending on the GW packet geometry; and (3) in the generation of secondary GWs that is due largely to transient momentum transport prior to GW dissipation for GW packets localized in 2-D or 3-D. These various dynamics cannot be described or parameterized using linear theory or models requiring slowly varying fields and GW parameters. Weakly nonlinear theory can provide valuable guidance in the absence of large amplitudes and instabilities [e.g., *Whitham*, 1974; *Grimshaw*, 1975, 1977; *Scinocca and Sutherland*, 2010], and 2-D models can reproduce the initial nonlinear evolution of a self-accelerating GW packet [e.g., *Sutherland*, 2001, 2006a; *Dosser and Sutherland*, 2011]. However, only fully nonlinear 3-D models are able to address the full range of SA dynamics for more general GW packets including the consequences of instabilities that impact momentum deposition and mean flow evolution. Unfortunately, there have been no previous observational studies that have identified SA dynamics to date of which we are aware.

Acknowledgments
The research described here was performed under NSF grants AGS-1261623 and AGS-1242943, ONR contract N0014-13-1-0488, and NASA contracts NNH12CC04C and NNX14AN51G. We also acknowledge the DoD High Performance Computing Modernization Program for valuable access to several supercomputer platforms that allowed the simulations reported here. Researchers wishing to obtain model results for collaborative research purposes should contact the lead author at dave@gats-inc.com, as model outputs are often too large to be placed on a community database, but can be prepared for use together with those wishing to pursue joint research.

References

Abdu, M. A., E. A. Kherani, I. S. Batista, E. R. de Paula, and D. C. Fritts (2009), An evaluation of the ESF/bubble irregularity growth conditions under gravity wave influences based on observational data from the SpreadFEx campaign, *Ann. Geophys.*, SpreadFEx special issue, *27*, 2607–2622.

Achatz, U. (2005), On the role of optimal perturbations in the instability of monochromatic gravity waves, *Phys. Fluids*, *17*, 094107, doi:10.1063/1.2046709.

Achatz, U. (2007), The primary nonlinear dynamics of modal and nonmodal perturbations of monochromatic inertia-gravity waves, *J. Atmos. Sci.*, *64*, 74–95.

Andreassen, Ø., P. Ø. Hvidsten, D. C. Fritts, and S. Arendt (1998), Vorticity dynamics in a breaking gravity wave: 1. Initial instability evolution, *J. Fluid Mech.*, *367*, 27–46.

Bannon, P. (1996), On the anelastic approximation for a compressible atmosphere, *J. Atmos. Sci.*, *53*, 3618–3628.

Djuth, F. T., M. P. Sulzer, J. H. Elder, and V. B. Wickwar (1997), High-resolution studies of atmosphere-ionosphere coupling at Arecibo Observatory, Puerto Rico, *Radio Sci.*, *32*, 2321–2344, doi:10.1029/97RS02797.

Djuth, F. T., M. P. Sulzer, S. A. Gonzales, J. D. Mathews, J. H. Elder, and R. L. Walterscheid (2004), A continuum of gravity waves in the Arecibo thermosphere?, *Geophys. Res. Lett.*, *31*, L16801, doi:10.1029/2003GL019376.

Dosser, H. V., and B. R. Sutherland (2011), Weakly nonlinear non-Boussinesq internal gravity wavepackets, *Phys. D*, *240*, 346–356.

Dunkerton, T. J. (1981), Wave transience in a compressible atmosphere. Part I: Transient internal wave, mean flow interaction, *J. Atmos. Sci.*, *38*, 281–297.

Felten, F. N., and T. S. Lund (2006), Kinetic energy conservation issues associated with the collocated mesh scheme for incompressible flow, *J. Comput. Phys.*, *215*, 465–484.

Franke, P. M., and W. A. Robinson (1999), Nonlinear behavior in the propagation of atmospheric gravity waves, *J. Atmos. Sci.*, *56*, 3010–3027, doi:10.1175/1520-0469(1999)056<3010:NBITPO>2.0.CO;2.

Fritts, D. C., and M. J. Alexander (2003), Gravity dynamics and effects in the middle atmosphere, *Rev. Geophys.*, *41*(1), 1003, doi:10.1029/2001RG000106.

Fritts, D. C., and T. J. Dunkerton (1984), A quasi-linear study of gravity wave saturation and self-acceleration, *J. Atmos. Sci.*, *41*, 3272–3289.

Fritts, D. C., and T. Lund (2011), Gravity wave influences in the thermosphere and ionosphere: Observations and recent modeling, in *Aeronomy of the Earth's Atmosphere and Ionosphere*, *IAGA Spec. Sopron Book Ser.*, vol. 2, edited by M. A. Abdu, D. Pancheva, and A. Bhattacharyya, pp. 109–130, Springer, New York.

Fritts, D. C., and G. D. Nastrom (1992), Sources of mesoscale variability of gravity waves, II: Frontal, convective, and jet stream excitation, *J. Atmos. Sci.*, *49*, 111–127.

Fritts, D. C., and S. L. Vadas (2008), Gravity wave penetration into the thermosphere: Sensitivity to solar cycle variations and mean winds, *Ann. Geophys.*, *26*, 3841–3861.

Fritts, D. C., and R. A. Vincent (1987), Mesospheric momentum flux studies at Adelaide, Australia: Observations and a gravity wave/tidal interaction model, *J. Atmos. Sci.*, *44*, 605–619.

Fritts, D. C., S. A. Smith, B. B. Balsley, and C. R. Philbrick (1988), Evidence of gravity wave saturation and local turbulence production in the summer mesosphere and lower thermosphere during the STATE experiment, *J. Geophys. Res.*, *93*, 7015–7025, doi:10.1029/JD093iD06p07015.

Fritts, D. C., J. R. Isler, G. E. Thomas, and Ø. Andreassen (1993), Wave breaking signatures in noctilucent clouds, *Geophys. Res. Lett.*, *20*, 2039–2042, doi:10.1029/93GL01982.

Fritts, D. C., J. F. Garten, and O. Andreassen (1996), Wave breaking and transition to turbulence in stratified shear flows, *J. Atmos. Sci.*, *53*, 1057–1085.

Fritts, D. C., S. A. Vadas, and Y. Yamada (2002), An estimate of strong local gravity wave body forcing based on OH airglow and meteor radar observations, *Geophys. Res. Lett.*, *29*(10), 1429, doi:10.1029/2001GL013753.

Fritts, D. C., L. Wang, J. Werne, T. Lund, and K. Wan (2009a), Gravity wave instability dynamics at high Reynolds numbers. 1: Wave field evolution at large amplitudes and high frequencies, *J. Atmos. Sci.*, *66*, 1126–1148, doi:10.1175/2008JAS2726.1.

Fritts, D. C., L. Wang, J. Werne, T. Lund, and K. Wan (2009b), Gravity wave instability dynamics at high Reynolds numbers. 2: Turbulence evolution, structure, and anisotropy, *J. Atmos. Sci.*, *66*, 1149–1171, doi:10.1175/2008JAS2727.1.

Fritts, D. C., L. Wang, and J. Werne (2013), Gravity wave—Fine structure interactions. Part 1: Energy dissipation evolutions, statistics, and implications, *J. Atmos. Sci.*, *70*(12), 3710–3734.

Fruman, M. D., S. Remmler, U. Achatz, and S. Hickel (2014), On the construction of a direct numerical simulation of a breaking inertia-gravity wave in the upper mesosphere, *J. Geophys. Res. Atmos.*, *119*, 11,613–11,640, doi:10.1002/2014JD022046.

Garcia, R. R., and B. Boville (1994), "Downward control" of the mean meridional circulation and temperature distribution of the polar winter stratosphere, *J. Atmos. Sci.*, *51*, 2238–2245.

Garcia, R. R., and S. Solomon (1985), The effect of breaking gravity waves on the dynamics and chemical composition of the mesosphere and lower thermosphere, *J. Geophys. Res.*, *90*, 3850–3868, doi:10.1029/JD090iD02p03850.

Gavrilov, N. M., and S. P. Kshevetskii (2015), Dynamical and thermal effects of nonsteady nonlinear acoustic-gravity waves propagating from tropospheric sources to the upper atmosphere, *Adv. Space Res.*, doi:10.1016/j.asr.2015.01.033.

Gavrilov, N. M., S. Fukao, and T. Nakamura (2000), Gravity wave intensity and momentum fluxes in the mesosphere over Shigaraki, Japan (35°N, 136°E) during 1986–1997, *Ann. Geophys.*, *18*, 834–843.

Grimshaw, R. H. J. (1975), Nonlinear internal gravity waves and their interaction with the mean wind, *J. Atmos. Sci.*, *32*, 1779–1793.

Grimshaw, R. H. J. (1977), The modulation of an internal gravity wave packet and the resonance with the mean motion, *Stud. Appl. Math*, *56*, 241–266.

Hasselmann, K. (1967), A criterion for non-linear wave stability, *J. Fluid Mech.*, *30*, 737–739.

Haynes, P. H., C. J. Marks, M. E. McIntyre, T. G. Shephard, and K. P. Shine (1991), On the "downward control" of extratropical diabatic circulations by eddy-induced mean zonal forces, *J. Atmos. Sci.*, *48*, 657–678.

Heale, C. J., J. B. Snively, M. P. Hickey, and C. J. Ali (2014), Thermospheric dissipation of upward propagating gravity wave packets, *J. Geophys. Res. Space Physics*, *119*, 3857–3872, doi:10.1002/2013JA019387.

Hines, C. O. (1960), Internal gravity waves at ionospheric heights, *Can. J. Phys.*, *38*(11), 1441–1481.

Hocke, K., and K. Schlegel (1996), A review of atmospheric gravity waves and traveling ionospheric disturbances: 1982–1995, *Ann. Geophys.*, *14*, 917–940.

Holton, J. R. (1982), The role of gravity wave induced drag and diffusion in the momentum budget of the mesosphere, *J. Atmos. Sci.*, *39*, 791–799.

Holton, J. R. (1983), The influence of gravity wave breaking on the general circulation of the middle atmosphere, *J. Atmos. Sci.*, *40*, 2497–2507.

Holton, J. R. (1984), The generation of mesospheric planetary waves by zonally asymmetric gravity wave breaking, *J. Atmos. Sci.*, *41*, 3427–3430.

Horinouchi, T., T. Nakamura, and J. Kosaka (2002), Convectively generated mesoscale gravity waves simulated throughout the middle atmosphere, *Geophys. Res. Lett.*, *29*(21), 2007, doi:10.1029/2002GL016069.

Innis, J. L., and M. Conde (2002), Characterization of acoustic–gravity waves in the upper thermosphere using Dynamics Explorer 2 Wind and Temperature Spectrometer (WATS) and Neutral Atmosphere Composition Spectrometer (NACS) data, *J. Geophys. Res.*, *107*(A12), 1418, doi:10.1029/2002JA009370.

Innis, J. L., P. A. Greet, and P. L. Dyson (2001), Evidence for thermospheric gravity waves in the southern polar cap from ground-based vertical velocity and photometric observations, *Ann. Geophys.*, *19*, 533–543.

Kim, Y.-J., S. D. Eckermann, and H.-Y. Chun (2003), A overview of the past, present and future of gravity-wave drag parameterization for numerical climate and weather prediction models, *Atmos. Ocean*, *41*, 65–98.

Klemp, J. B., and D. E. Durran (1983), An upper boundary condition permitting internal gravity wave radiation in numerical mesoscale models, *Mon. Weather Rev.*, *111*, 430–444.

Klostermeyer, J. (1991), Two- and three-dimensional parametric instabilities in finite amplitude internal gravity waves, *Geophys. Astrophys. Fluid Dyn.*, *61*, 1–25.

Lighthill, M. J. (1978), *Waves in Fluids*, Cambridge Univ. Press, Cambridge, U. K.

Lindzen, R. S. (1981), Turbulence and stress owing to gravity wave and tidal breakdown, *J. Geophys. Res.*, *86*, 9707–9714, doi:10.1029/JC086iC10p09707.

Lipps, F. B. (1990), On the anelastic approximation for deep convection, *J. Atmos. Sci.*, *47*, 1794–1798.

Lipps, F. B., and R. S. Hemler (1982), A scale analysis of deep moist convection and some associated numerical calculations, *J. Atmos. Sci.*, *39*, 2192–2210.

Liu, X., J. Xu, and H.-L. Liu (2008), Nonlinear interactions between gravity waves with different wavelengths and diurnal tide, *J. Geophys. Res.*, *113*, D08112, doi:10.1029/2007JD009136.

Lombard, P. N., and J. J. Riley (1996), On the breakdown into turbulence of propagating internal waves, *Dyn. Atmos. Ocean.*, *23*, 345–355.

Lu, W., and D. C. Fritts (1993), Spectral estimates of gravity wave energy and momentum fluxes. Part III: Gravity wave-tidal interactions, *J. Atmos. Sci.*, *50*, 3714–3727, doi:10.1175/1520-0469(1993)050<3714:SEOGWE>2.0.CO;2.

Lund, T., and D. C. Fritts (2012), Gravity wave breaking and turbulence generation in the thermosphere, *J. Geophys. Res.*, *117*, D21105, doi:10.1029/JD017536.

Luo, Z., and D. C. Fritts (1993), Gravity wave excitation by geostrophic adjustment of the jet stream. Part II: Three-dimensional forcing, *J. Atmos. Sci.*, *50*, 104–115.

Mayr, H. G., I. Harris, F. A. Herrero, N. W. Spencer, F. Varosi, and W. D. Pesnell (1990), Thermospheric gravity waves: Observations and interpretation using the transfer function model (TFM), *Space Sci. Rev.*, *54*, 297–375, doi:10.1007/BF00177800.

McComas, C. H., and F. P. Bretherton (1977), Resonant interaction of oceanic internal waves, *J. Geophys. Res.*, *82*, 1397–1412, doi:10.1029/JC082i009p01397.

McLandress, C., and W. E. Ward (1994), Tidal/gravity wave interactions and their influence on the large-scale dynamics of the middle atmosphere: Model results, *J. Geophys. Res.*, *99*, 8139–8156, doi:10.1029/94JD00486.

Mendillo, M., J. Baumgardner, D. Nottingham, J. Aarons, B. Reinisch, J. Scali, and M. Kelley (1997), Investigation of thermospheric-ionospheric dynamics with 6300-Å images from the Arecibo Observatory, *J. Geophys. Res.*, *102*(A4), 7331–7343, doi:10.1029/96JA02786.

Meyer, C. K. (1999a), Gravity wave interactions with the diurnal propagating tide, *J. Geophys. Res.*, *104*, 4223–4239, doi:10.1029/1998JD200089.

Meyer, C. K. (1999b), Gravity wave interactions with mesospheric planetary waves: A mechanism for penetration into the thermosphere-ionosphere system, *J. Geophys. Res.*, *104*, 28,181–28,196, doi:10.1029/1999JA900346.

Mied, R. R. (1976), The occurrence of parametric instabilities in finite-amplitude internal gravity waves, *J. Fluid Mech.*, *78*, 763–784.

Miyahara, S., and J. M. Forbes (1991), Interactions between gravity waves and the diurnal tide in the mesosphere and lower thermosphere, *J. Meteorol. Soc. Jpn.*, *69*, 523–531.

Müller, P., G. Holloway, F. Henyey, and N. Pomphrey (1986), Nonlinear interactions among internal gravity waves, *Rev. Geophys.*, *24*, 493–536, doi:10.1029/RG024i003p00493.

Nastrom, G. D., B. B. Balsley, and D. A. Carter (1982), Mean meridional winds in the mid- and high-latitude summer mesosphere, *Geophys. Res. Lett.*, *9*, 139–142, doi:10.1029/GL009i002p00139.

Oberheide, J., K. Shiokawa, S. Gurubaran, W. E. Ward, H. Fujiwara, M. J. Kosch, J. J. Makela, and H. Takahashi (2015), The geospace response to variable inputs from the lower atmosphere: A review of the progress made by Task Group 4 of CAWSES-II, *Prog. Earth Planet. Sci.*, *2*, doi:10.1186/s40645-014-0031-4.

Oliver, W. L., Y. Otsuka, M. Sato, T. Takami, and S. Fukao (1997), A climatology of F region gravity wave propagation over the middle and upper atmosphere radar, *J. Geophys. Res.*, *102*, 14,499–14,512, doi:10.1029/97JA00491.

Ortland, D. A., and M. J. Alexander (2006), Gravity wave influence on the global structure of the diurnal tide in the mesosphere and lower thermosphere, *J. Geophys. Res.*, *111*, A10S10, doi:10.1029/2005JA011467.

Pitteway, M. L. V., and C. O. Hines (1963), The viscous damping of atmospheric gravity waves, *Can. J. Phys.*, *41*, 1935–1948.

Preusse, P., S. D. Eckermann, J. Oberheide, M. E. Hagan, and D. Offermann (2001), Modulation of gravity waves by tides as seen in CRISTA temperatures, *Adv. Space Res.*, *27*(10), 1773–1778, doi:10.1016/S0273(01)0336-2.

Rieper, F., U. Achatz, and R. Klein (2013), Range of validity of an extended WKB theory for atmospheric gravity waves: One dimensional and two-dimensional case, *J. Fluid Mech.*, *729*, 330–363, doi:10.1017/jfm.2013.307.

Scinocca, J. F., and B. R. Sutherland (2010), Self-acceleration in the parameterization of orographic gravity wave drag, *J. Atmos. Sci.*, *67*, 2537–2546.

Smith, A. K. (1996), Longitudinal variations in mesospheric winds: Evidence for gravity wave filtering by planetary waves, *J. Atmos. Sci.*, *53*, 1156–1173, doi:10.1175/1520-0469(1996)053<1156:LVIMWE>2.0.CO;2.

Snively, J. B., and V. P. Pasco (2003), Breaking of thunderstorm-generated gravity waves as a source of short-period ducted waves at mesopause altitudes, *Geophys. Res. Lett.*, *30*(24), 2254, doi:10.1029/2003GL018436.

Sonmor, L. J., and G. P. Klaassen (1997), Toward a unified theory of gravity wave stability, *J. Atmos. Sci.*, *54*(22), 2655–2680.

Sutherland, B. R. (1999), Propagation and reflection of internal waves, *Phys. Fluids*, *11*(5), 1081–1090.

Sutherland, B. R. (2001), Finite-amplitude internal wavepacket dispersion and breaking, *J. Fluid Mech.*, *429*, 343–380.

Sutherland, B. R. (2006a), Weakly nonlinear internal gravity wavepackets, *J. Fluid Mech.*, *569*, 249–258.

Sutherland, B. R. (2006b), Internal wave instability: Wave-wave versus wave-induced mean flow interactions, *Phys. Fluids*, *18*, 074107, doi:10.1063/1.2219102.

Tsuda, T., Y. Murayama, M. Yamamoto, S. Kato, and S. Fukao (1990), Seasonal variation of momentum flux in the mesosphere observed with the MU radar, *Geophys. Res. Lett.*, *17*, 725–728, doi:10.1029/GL017i006p00725.

Vadas, S. L. (2007), Horizontal and vertical propagation, and dissipation of gravity waves in the thermosphere from lower atmospheric and thermospheric sources, *J. Geophys. Res.*, *112*, A06305, doi:10.1029/2006JA011845.

Vadas, S. L., and D. C. Fritts (2001), Gravity wave radiation and mean responses to local body forces in the atmosphere, *J. Atmos. Sci.*, *58*, 2249–2279.

Vadas, S. L., and D. C. Fritts (2002), The importance of spatial variability in the generation of secondary gravity waves from local body forces, *Geophys. Res. Lett.*, *29*(20), 1984, 10.1029/2002GL015574.

Vadas, S. L., and D. C. Fritts (2005), Thermospheric responses to gravity waves: Influences of increasing viscosity and thermal diffusivity, *J. Geophys. Res.*, *110*, D15103, doi:10.1029/2004JD005574.

Vadas, S. L., and D. C. Fritts (2004), Thermospheric responses to gravity waves arising from mesoscale convective complexes, *J. Atmos. Solar Terres. Phys.*, *66*, 781–804.

Vadas, S. L., and H.-L. Liu (2009), The generation of large-scale gravity waves and neutral winds in the thermosphere from the dissipation of convectively-generated gravity waves', *J. Geophys. Res.*, *114*, A10310, doi:10.1029/2009JA014108.

Vadas, S. L., and H.-L. Liu (2011), Neutral winds and densities at the bottomside of the F layer from primary and secondary gravity waves from deep convection, in *Aeronomy of the Earth's Atmosphere and Ionosphere, IAGA Spec. Sopron Book Ser.*, vol. 2, edited by M. A. Abdu, D. Pancheva, and A. Bhattacharyya, pp. 131–139, Springer, New York.

Vadas, S. L., and H.-L. Liu (2013), The large-scale neutral and plasma responses to the body forces created by the dissipation of gravity waves from 6 hours of deep convection in Brazil, *J. Geophys. Res. Space Physics*, *118*, 1–25, doi:10.1002/jgra.50249.

Vadas, S. L., and M. Nicolls (2009), Temporal evolution of neutral, thermospheric winds and plasma response using PFISR measurements of gravity waves, *J. Atmos. Sol. Terr. Phys.*, *71*, 740–770.

Vanneste, J. (1995), The instability of internal gravity waves to localized disturbances, *Ann. Geophys.*, *13*, 196–210.

Vincent, R. A., and I. M. Reid (1983), HF Doppler measurements of mesospheric momentum fluxes, *J. Atmos. Sci.*, *40*, 1321–1333.

Walterscheid, R. L. (1981), Inertio-gravity wave induced accelerations of mean flow having an imposed periodic component: Implications for tidal observations in the meteor region, *J. Geophys. Res.*, *86*, 9698–9706, doi:10.1029/JC086iC10p09698.

Wang, D.-Y., and D. C. Fritts (1991), Evidence of gravity wave–tidal interaction observed near the summer mesopause at Poker Flat, Alaska, *J. Atmos. Sci.*, *48*, 572–583, doi:10.1175/1520-0469(1991)048<0572:EOGWIO>2.0.CO;2.

White, F. M. (1974), *Viscous Fluid Flow*, McGraw-Hill, New York.

Whitham, G. B. (1965), A general approach to linear and nonlinear dispersive waves using a Lagrangian, *J. Fluid Mech.*, *22*, 273–283.

Whitham, G. B. (1974), *Linear and Nonlinear Waves*, John Wiley, New York.

Yeh, K. C., and C. H. Liu (1981), The instability of atmospheric gravity waves through wave-wave interactions, *J. Geophys. Res.*, *86*(C10), 9722–9728, doi:10.1029/JC086iC10p09722.

Yiğit, E., and A. S. Medvedev (2010), Internal gravity waves in the thermosphere during low and high solar activity: Simulation study, *J. Geophys. Res.*, *115*, A00G02, doi:10.1029/2009JA015106.

Yiğit, E., and A. S. Medvedev (2015), Internal wave coupling processes in Earth's atmosphere, *Adv. Space Res.*, *55*, 983–1003, doi:10.1016/j.asr.2014.11.020.

Yiğit, E., A. D. Aylward, and A. S. Medvedev (2008), Parameterization of the effects of vertically propagating gravity waves for thermosphere general circulation models: Sensitivity study, *J. Geophys. Res.*, *113*, D19106, doi:10.1029/2008JD010135.

Yiğit, E., A. S. Medvedev, A. D. Aylward, P. Hartogh, and M. J. Harris (2009), Modeling the effects of gravity wave momentum deposition on the general circulation above the turbopause, *J. Geophys. Res.*, *114*, D07101, doi:10.1029/2008JD011132.

Yiğit, E., A. S. Medvedev, S. L. England, and T. J. Immel (2014), Simulated variability of the high-latitude thermosphere induced by small-scale gravity waves during a sudden stratospheric warming, *J. Geophys. Res. Space Physics*, *119*, 357–365, doi:10.1002/2013JA019283.